CHALMERS UNIVERSITY OF TECHNOLOGY
Gothenburg, Sweden
www.chalmers.se

CHALMERS
UNIVERSITY OF TECHNOLOGY

LICENTIATE THESIS

JUAN CABELLO SÁNCHEZ

JUAN CABELLO SÁNCHEZ • On-chip terahertz characterisation of liquids • 2020

On-chip terahertz characterisation of liquids

JUAN CABELLO SÁNCHEZ

CHALMERS
UNIVERSITY OF TECHNOLOGY

DEPARTMENT OF MICROTECHNOLOGY AND NANOSCIENCE - MC2
CHALMERS UNIVERSITY OF TECHNOLOGY
Gothenburg, Sweden 2020
www.chalmers.se

THESIS FOR THE DEGREE OF LICENTIATE OF ENGINEERING

On-chip terahertz characterisation of liquids

Juan Cabello Sánchez

CHALMERS
UNIVERSITY OF TECHNOLOGY

Department of Microtechnology and Nanoscience - MC2
Chalmers University of Technology
Gothenburg, Sweden, 2020

On-chip terahertz characterisation of liquids

Juan Cabello Sánchez

ORCID: 0000-0002-9821-3199

Technical Report No. MC2-434
ISSN 1652-0769
This thesis has been prepared using LaTeX.

Department of Microtechnology and Nanoscience - MC2
Chalmers University of Technology
SE-412 96 Gothenburg, Sweden
Phone: +46 (0)31 772 1000
www.chalmers.se

Printed by Chalmers Reproservice
Gothenburg, Sweden, November 2020

If you wish to strive for peace of soul and happiness, then believe;
if you wish to be a disciple of truth, then inquire.

Abstract

Spectroscopy at terahertz frequencies can be used in a wide range of applications including radio-astronomy, pharmaceutical manufacturing control, and the study of processes in molecular biology. Biomolecular samples should preferably be studied in their native environment, water, however, water poses extreme attenuation for THz-frequency waves, deteriorating or even impeding analysis using these waves. The most common THz spectroscopy method, time-domain spectroscopy, can measure water samples using free-space measurements, lacks sensitivity when trying to measure on a chip environment. To exploit the advantages that chip measurements offer, such as integration and cost, this thesis works on developing on-chip THz spectroscopy of aqueous samples using a frequency-domain approach, with vector network analysers. Vector network analysers exhibit a higher dynamic range than time-domain spectroscopy systems, making them a promising alternative for sensitive THz measurements. For maximising the sensitivity of the measurements, the losses must be minimised. One important source of losses at THz frequencies are conductor and radiation loss. In this thesis, two planar waveguides were designed, coplanar waveguide and planar Goubau line, minimising their losses at THz frequencies by avoiding the coupling to other parasitic modes, obtaining attenuation constants as low as 0.85 Np/mm for coplanar waveguide and 0.33 Np/mm for planar Goubau line. Additionally, planar Goubau line calibration structures were developed for setting the measurement plane along this planar waveguide. Finally, coplanar waveguides were integrated with microfluidic channels to perform spectroscopy measurements of water samples, showing good performances as THz sensors of high-loss liquids.

This thesis is a first step towards a sensitive and miniaturised system for measuring the electrical properties of high-loss liquids, which could shed light on the fundamental biomolecular processes in the picosecond time-scale.

Keywords: Chip, coplanar waveguides (CPW), isopropyl alcohol (IPA), liquids, material properties, microfluidic channels, on-wafer measurements, dielectric permittivity, planar Goubau line, Through-Reflect-Line (TRL) calibration, scattering parameters, terahertz spectroscopy, vector network analyzers (VNA), water

List of publications

The following papers constitute the main work for this thesis:

[A] **J. Cabello-Sánchez**, H. Rodilla, V. Drakinskiy and J. Stake, "Multi-line TRL Calibration Standards for S-parameter Measurement of Planar Goubau Lines from 0.75 THz to 1.1 THz," in proceedings of the *2018 IEEE/MTT-S International Microwave Symposium - IMS*, Philadelphia, PA, 2018, pp. 879-882, doi: 10.1109/MWSYM.2018.8439138.

[B] **J. Cabello-Sánchez**, H. Rodilla, V. Drakinskiy, and J. Stake, "Transmission Loss in Coplanar Waveguide and Planar Goubau Line between 0.75 THz and 1.1 THz," in proceedings of the *43rd International Conference on Infrared, Millimeter, and Terahertz Waves (IRMMW-THz)*, Nagoya, 2018, pp. 1–2, doi: 10.1109/IRMMW-THz.2018.8510326.

[C] **J. Cabello-Sanchez**, V. Drakinskiy, J. Stake and H. Rodilla, "On-Chip Characterization of High-Loss Liquids between 750 GHz and 1100 GHz," in *IEEE Transactions on Terahertz Science and Technology*, Vol. 11, No. 1, Jan. 2021, doi: 10.1109/TTHZ.2020.3029503.

Acknowledgments

First and foremost I would like to thank my main supervisor, Helena Rodilla, for the guidance, support and fruitful and interesting discussions that I've had with her. Secondly, to my co-supervisor Jan Stake, who has a long-time expertise in the field, and as an editor-in-chief, which from I learnt a lot about writing and publishing. Big thanks also to Vladimir, which apart from being great to count with his expertise in nano-fabrication, I enjoyed talking to him during lunch breaks and exchange different perspectives. Also to Mats Myremark for his great help on his ingenious solutions for my measurement setup and for the great vibe he has. Of course, a big mention to my dear office mates, Anis, Divya and Peter who not only I have learned a lot from discussions we had, but also feel very lucky to enjoy their company on my everyday life. Divya is my LaTeX guru, so I can only be grateful for all the things I've learned from her. Same goes for the rest of my TML colleagues (Xinxin, Marlene, Marijana, Mohamed, Junjie, Sergei, etc.) and MEL colleagues (Ahmed, Olivier, Vessen, Frida, etc.). Regarding people not related to my work—but still deserve mention—I would like to give big thanks to my family (I am who I am greatly because of them), my bike-loving long-lasting *sambo* Lucas, my ETSIT-UPM friends (for those amazing discussions covering science, philosophy and other unspeakable topics), my brother from another mother Simon, and other friends.

This work was supported by the Swedish Research Council (Vetenskapsrådet) under grant 2015-03981, and Knut and Alice Wallenberg Foundation under grant 2014.0275.

Acronyms

CPW:	Coplanar Waveguide
DUT:	Device Under Test
FTIR:	Fourier-Transform Infrared spectroscopy
GSG:	Ground-Signal-Ground
IF:	Intermediate Frequency
IPA:	Isopropyl Alcohol
LO:	Local Oscillator
PDMS:	Polydimethylsiloxane
PE:	Polyethene
PET:	Polyethylene Terephthalate
PGL:	Planar Goubau Line
RF:	Radio-Frequency
SNR:	Signal-to-Noise Ratio
SOLT:	Short Open Load Through
TDS:	Time-Domain Spectroscopy
TE:	Transverse Electric
TEM:	Transverse Electromagnetic
TM:	Transverse Magnetic
TRL:	Through-Reflect-Line
VNA:	Vector Network Analyzer

Mathematical symbols

a	Bruggeman model curve fitting factor
C	Capacitance
c	Speed of light in vacuum
d	Substrate thickness
$\vec{E}$	Electric field
f	Frequency
G	Conductance
$\vec{H}$	Magnetic field
I	Current
j	Imaginary unit, $\sqrt{-1}$
k_0	Wavenumber in vacuum
L	Inductance
$\hat{n}$	Complex refractive index
n'	Real refractive index
R	Resistance
S_{ij}	S-parameter from port j to port i.
s	Strip width (CPW and PGL)
T	Transfer scattering matrices
V	Voltage
v	Volume concentration
w	Gap width (CPW)
Z_c	Characteristic impedance
α	Attenuation constant
β	Phase constant
γ	Propagation constant
δ	Loss tangent
$\hat{\epsilon}$	Complex dielectric permittivity
ϵ'	Real part of dielectric permittivity
ϵ''	Imaginary part of dielectric permittivity
ϵ_0	Dielectric permittivity of vacuum
κ	Imaginary part of refractive index
λ	Wavelength

λ_0	Wavelength in vacuum
μ_0	Magnetic permeability of vacuum
τ	Relaxation time
ω	Angular frequency
ω_0	Resonant angular frequency
ω_p	Plasma angular frequency

Contents

CHAPTER 1

Introduction

Terahertz (THz) waves, spanning between 0.3 THz and 10 THz in the electromagnetic spectrum, lie between the microwave and infrared bands. Traditionally, THz technology has been used in astronomy for detecting light-weight molecules [1], making this discipline an important driver for THz technology in the early days. As new instrumentation was developed, the application of THz waves expanded to many other fields, including high-speed communications [2], pharmaceutical control [3], security [4] and medicine and biology [5].

In the field of biology, THz waves have proven to have a unique interaction with biomolecules, since the existence of low-frequency motions of biomolecules at THz frequencies are believed to play a key role in their biological function [6]. Measuring these vibrational modes could give valuable information about the conformational dynamics of the biomolecules and could be used for their study and identification [7], [8]. THz spectroscopy has succeeded in analysing protein structure dynamics [6], bio-affinity between biomolecules [9] and characterising genetic material [10], showing high sensitivity while being label-free. Label-free techniques have the advantage of not needing labelling preparatory steps and eliminate the influence of the chemical labels in

the measured samples [11].

Traditionally, the most extended technique in THz spectroscopy was Time-Domain Spectroscopy (TDS) [12], with a photonic approach to THz wave generation. It generates short and coherent THz pulses by pumping a semiconductor crystal with femtosecond optical pulses and resolves the magnitude and phase response in the time domain by using a phase translation. This method has the advantage of being broadband and having relatively high dynamic range. However, it has the disadvantage of having typically low signal-to-noise ratios [13], which limits the minimum detectable signal change and has a bulky set-up which requires careful alignment of the optical components. Despite this, TDS is a method which has succeeded in doing broadband THz spectroscopy of high-loss aqueous samples (with losses in the order of 100 dB/mm) in transmission-mode [14], reflection-mode [15], and on-chip set-ups [16], [17]. Regardless of their achievements and as a consequence of an insufficient measurement signal-to-noise ratio (SNR), TDS on-chip setups could either not resolve samples with a water concentration higher than 60% at frequencies higher than 0.5 THz [17], or required keeping the sample away from the region with the most field intensity in the planar waveguide used [16], deteriorating sensitivity to sample changes. For resolving samples and achieve higher sensitivities to sample changes, a higher SNR needs to be achieved.

TDS is a mature technology which is not likely to make technological breakthroughs which could offer a drastic enhancement of the SNR of the measurements. However, recent advances in heterodyne technology now allow the use of the microwave-based approach using vector network analysers (VNA) in THz spectroscopy measurements. Compared to the photonic-based THz-TDS, VNAs have higher dynamic range [18], traceability to the International System of Units [19], first-rate spectral resolution (~ 1 Hz), can use calibration methods [20], and has a relatively compact measurement setup. The downside of using VNAs is that its frequency span is limited by the rectangular waveguide bands at THz frequencies, thus having narrower bandwidths than THz-TDS for a given setup. In addition to recent VNA developments at THz frequencies, ground-signal-ground (GSG) RF-probes have been developed up to 1.1 THz [21] for VNAs, enabling a quick and reliable method for measuring chips at THz frequencies, and developing integrated solutions. Using contact probes also has the advantage of being more power-efficient than free-space coupling of the field into the measured chip. These advantages may give VNA-

based THz spectroscopy higher sensitivity over THz-TDS, could increase the maximum frequency of these type of devices which have already been studied at microwaves and millimetre-wave frequencies [22]–[24], and could open new possibilities for detecting subtle biomolecular changes [25].

This thesis has tackled the challenges of the design, fabrication and measurements of chips used for THz spectroscopy of high-loss aqueous samples while trying to maximise their sensitivity. For this, two on-chip liquid sensors based on coplanar waveguide (CPW) and planar Goubau line (PGL) have been designed, fabricated and compared in the 0.75 THz to 1.1 THz frequency range. The chips were integrated with microfluidic channels to deliver the liquid samples to the sensing area and controlling their volume. Both CPW and PGL were designed to minimise their losses by using ultra-thin substrates which avoids power leakage to other undesirable substrate modes. Calibration standards were designed and integrated into the device's chip for both CPW and PGL, making it possible to have the measurement plane in each planar waveguide. No PGL calibration standards existed to the best of the author's knowledge, so a wide-band PGL Reflect standard was developed which enables Through-Reflect-Line calibration in this waveguide. These developments are a first step towards an integrated and high-sensitivity THz spectroscopy solution for high-loss aqueous samples.

The thesis begins with a broad background of relevant concepts in chapter 2. Chapter 3 describes the design and fabrication of the devices, and the sample characterisation method used. Chapter 4 presents measurements validating the developed PGL calibration standards, loss comparison of the designed CPW and PGL, and measurements of the CPW as a liquid sample sensor. Finally, chapter 5 presents conclusions of the thesis and suggestions for future work.

CHAPTER 2

Background

This chapter describes basic concepts for on-chip THz characterization of liquids. It covers models for material properties (Sec. 2.1), THz spectroscopy and methods (Sec. 2.2), uncertainty and calibration techniques of scattering parameters (Sec. 2.3), wave propagation model (Sec. 2.4), description of planar transmission lines (Sec. 2.5) and single-wire waveguides (Sec. 2.6), substrate modes (Sec. 2.7), and finally extraction techniques of material properties (Sec. 2.8).

2.1 Modeling of material properties

There are several ways to express the frequency dependence of the electrical properties of materials. Two commonly used models are the Debye and Lorentz models.

The Debye model expresses the frequency dependence of the permittivity close to a resonance by describing the permittivity values at the higher, ϵ_∞, and lower, ϵ_l, frequencies and the characteristic relaxation time of the material,

τ. It is given by the equation:

$$\hat{\epsilon}(\omega) = \epsilon_{\infty}^{'} + \frac{\epsilon_{l}^{'} - \epsilon_{\infty}^{'}}{1 + j\omega\tau} \tag{2.1}$$

In the Lorentz model, the frequency dependence of the permittivity close to a resonance is characterised with the plasma angular frequency, ω_p, the undamped resonant angular frequency, ω_0, and the damping ratio, ζ. It is given by the equation:

$$\frac{\hat{\epsilon}}{\epsilon_0} = 1 + \frac{\omega_p^2}{(\omega_0^2 - \omega^2) + j\omega\zeta} \tag{2.2}$$

The properties of a dielectric can also be expressed as the complex refractive index, $\hat{n}$, which is related to the permittivity as:

$$\hat{n} = n^{'} - j\kappa = \sqrt{\hat{\epsilon}} = \sqrt{\epsilon^{'} - j\epsilon^{''}} \tag{2.3}$$

being $n^{'}$ and κ the real and imaginary parts of the refractive index. An advantage of of the complex refractive index over the complex dielectric permittivity is that the real and imaginary parts of the refractive index, $n^{'}$ and κ, correspond to only phase and magnitude changes, respectively, according to:

$$\hat{n} = \frac{\gamma}{jk_0} \tag{2.4}$$

where $\gamma = \alpha + j\beta$ is the propagation constant. In contrast, the assumption that $\epsilon^{'}$ corresponds to phase changes and $\epsilon^{''}$ corresponds to magnitude changes can only be approximated for low-loss cases.

2.1.1 Permittivity of material mixtures

Given two materials with permittivities ϵ_1, and ϵ_2, it is interesting to model the permittivity of a mixture, ϵ_m versus the volume concentration of, for example, the first material, v_1. Two useful formulas are the Bruggeman equation [26]:

$$\left[\frac{\epsilon_m - \epsilon_1}{\epsilon_2 - \epsilon_1}\right]\left[\frac{\epsilon_2}{\epsilon_m}\right]^{1/3} = 1 - v_1 \tag{2.5}$$

and the Böttcher equation [27]:

$$v_1 = \frac{(\epsilon_m - \epsilon_2)(2\epsilon_m + \epsilon_1)}{3\epsilon(\epsilon_1 - \epsilon_2)} \tag{2.6}$$

In the case of mixtures of two polar liquids, such as water and alcohols, Bruggeman's equation can be modified to fit mixtures of polar liquids, according to equation [28]:

$$\left[\frac{\epsilon_m - \epsilon_1}{\epsilon_2 - \epsilon_1}\right]\left[\frac{\epsilon_2}{\epsilon_m}\right]^{1/3} = 1 - \left[a - (a-1)v_1\right]v_1 \tag{2.7}$$

where a is a curve fitting parameter which accounts for the change in the orientation of the solvent molecules in the mixed solution.

2.2 THz-spectroscopy

Spectroscopy is the study of the interaction between electromagnetic waves and matter versus frequency. There are several methods for doing THz spectroscopy measurements, the three main ones are Fourier-transform spectroscopy, time-domain spectroscopy (THz-TDS) and continuous-wave spectroscopy.

2.2.1 Fourier-transform spectroscopy

Fourier-transform spectroscopy [29] is a technique which uses interferometry principles to obtain an interference pattern as a function of the position of a movable mirror. The interference pattern is then Fourier-transformed into the absorption spectrum of the sample under test. Far-infrared Fourier-transform spectroscopy has the advantage of being ultra-wide bandwidth from (sub-THz to mid-IR), and having high SNR above 3 THz, at least 33 dB. [30]. Whereas it has the disadvantages of being a non-coherent method in the far-infrared spectrum [31], having relatively low dynamic range (~40 dB) and lacking calibration techniques.

2.2.2 THz Time-domain spectroscopy

In THz-TDS, materials are analysed by short THz pulses which are sampled coherently in the time domain. THz pulses are generated by pumping

a photoconductive switch made with a semiconductor crystal with a short femtosecond optical pulse [32]. This causes an increase in conductivity in the crystal, producing a picosecond current pulse which excites an antenna, or it is coupled into a planar waveguide. The pulse interacts with the sample under test and is sampled in the time domain by using a delay line which introduces a variable delay between the pump and probe pulses.

It has the advantages of being a coherent method, having a large bandwidth of analysis, high dynamic range (~80 dB at 1 THz), and capable of frequency traceability [33]. Some disadvantages are that it consists of a bulky setup, requires careful alignment of optical elements and purging water vapour from setup, has low SNR (around 30 dB), lacks power traceability[31], and lacks calibration methods.

2.2.3 Continuous-wave terahertz spectroscopy

In this method, a continuous-wave hits a sample and the reflected or/and transmitted signals are measured. Continuous-wave spectroscopy can be made with both optical and electronic approaches. The optical approach uses photomixers, which focuses two lasers into a semiconductor crystal producing a THz beatnote, which excites an antenna. It has the advantage of covering a wide bandwidth from 0.3 THz to 3 THz but has low output power, around 10 nW. The electronic approach uses a frequency-swept sinusoidal signal which is multiplied in frequency obtaining a THz signal and uses heterodyne receivers for the detection. The most important electronic instrument using the heterodyne principle is the vector network analyser (VNA). VNAs characterise radio-frequency electronics devices in both magnitude and phase of both the transmitted and reflected waves. It has the advantages of being a coherent method, having a high dynamic range, high SNR [18], traceability to the international system of units [19], capable of using calibration techniques to move the measurement reference plane [20], and having first-class frequency resolution. Whereas it has the disadvantage of being limited to rectangular waveguide bands when measuring at THz frequencies, and that current technology has a maximum frequency of analysis of 1.5 THz [34]. VNAs generate THz continuous waves by using frequency multipliers to do a frequency up-conversion of microwave continuous waves, based on the generation of harmonics in non-linear devices [35]. As opposed to TDS, VNAs measures in the frequency domain using a heterodyne detector. The main advantage of the

heterodyne technique is that a signal can be converted to a lower intermediate frequency (IF), where the amplifying of the signal and the filtering of the noise can be done with greater performance, obtaining high SNRs. For example, when measuring THz signals using VNA can use an IF bandwidth of 50 Hz, minimising noise power.

2.3 Scattering parameters

At high frequencies, devices are usually characterised by measuring reflected and transmitted waves, normalised to an incident wave, in a linear and time-invariant regime. The magnitude and phase relations calculated between a device's ports are called scattering parameters, or S-parameters, and are defined as follows:

$$S_{ij} = \left.\frac{V_i^-}{V_j^+}\right|_{V_{k\neq j}^+=0} \tag{2.8}$$

where V_i^- is the reflected wave phasor in port i, V_j^+ is the incident wave phasor in port j. Note that this definition requires no incident waves in any other port other than j. Then, for a two-port S-parameters, we have:

$$\begin{pmatrix} V_1^- \\ V_2^- \end{pmatrix} = \begin{pmatrix} S_{11} & S_{12} \\ S_{21} & S_{22} \end{pmatrix} \begin{pmatrix} V_1^+ \\ V_2^+ \end{pmatrix} \tag{2.9}$$

For passive elements, the sum of the power of the reflected and transmitted waves cannot be higher than the incident wave, thus for a two-port device we have:

$$\sum_{i=1}^{2} \left|S_{ij}\right|^2 \leq 1 \quad \text{for } j = 1, 2 \tag{2.10}$$

If the two-port device is symmetrical between the ports, then:

$$S_{11} = S_{22} \tag{2.11}$$

And if the device doesn't contain any anisotropic materials it will reciprocal, and thus:

$$S_{ij} = S_{ji} \tag{2.12}$$

Current technology allows measuring S-parameters up to 1.5 THz with a

VNA [34], having rectangular hollow waveguides as output ports, which can measure waveguide blocks, or free-space measurements using horn antennas. Because of this, VNA measurements at these frequencies are limited to the rectangular waveguide bands. It is also possible to perform on-wafer measurements up to 1.1 THz by using ground-signal-ground probes [21], which offer a power-efficient method for coupling the signals to the chip.

2.3.1 Uncertainty in S-parameter measurements

Expressing complex S-parameters in magnitude and phase is intuitive as magnitude represents the signal attenuation and phase represents the time delay. But calculating uncertainty in magnitude and phase can introduce systematic errors in the data analysis for signals with low SNR, and hence S-parameters should be analyzed in terms of real and imaginary components [36]. The mean of the real and imaginary parts of the S-parameters can be calculated according to:

$$\begin{aligned} \overline{\mathrm{Re}(S)} &= \frac{1}{n}\sum_{i=1}^{n}\mathrm{Re}(S_i) \\ \overline{\mathrm{Im}(S)} &= \frac{1}{n}\sum_{i=1}^{n}\mathrm{Im}(S_i) \end{aligned} \tag{2.13}$$

and the standard deviations of the real and imaginary parts of the S-parameters can be calculated according to:

$$\begin{aligned} s(\overline{\mathrm{Re}(S)}) &= \sqrt{\frac{1}{n(n-1)}\sum_{i=1}^{n}\left(\mathrm{Re}(S_i) - \overline{\mathrm{Re}(S)}\right)^2} \\ s(\overline{\mathrm{Im}(S)}) &= \sqrt{\frac{1}{n(n-1)}\sum_{i=1}^{n}\left(\mathrm{Im}(S_i) - \overline{\mathrm{Im}(S)}\right)^2} \end{aligned} \tag{2.14}$$

2.3.2 S-parameter calibration techniques

An advantage of S-parameter measurements using a VNA is the capability to use calibration methods to correct systematic errors of the setup and move the measurement plane to a point of interest [20], effectively neglecting the effects of the circuit elements behind the measurement plane. Two-port calibration

methods consist of measuring at least three specific known standards to calculate the response of the circuit elements behind the measurement plane, which are de-embedded afterwards. Different calibration methods exist, each of them using different standards for resolving the measurement setup error parameters. Some commonly used methods are:

- Short-Open-Load-Through (SOLT): a traditional calibration which uses three reflection standards on each port and one transmission standard connecting the ports. The calibration plane lies in the location where standards are attached to the rectangular waveguides. It requires accurate modelling of the four calibration standards.

- Through-Reflect-Line (TRL): it has the advantage of having higher accuracy than SOLT calibration, needing only three calibration standards and not requiring loads or matches—which are hard to accurately fabricate for THz frequencies—thereby being more suitable for THz frequencies. The calibration plane lies in the middle of the Through standard, and thus in on-wafer measurements, the probe-tip transition is de-embedded, making it more accurate than calibrations which do not [37]. It does not require fully known standards [38] for solving the 12-term procedure [39], [40]. This method requires having a single mode propagating in the Through standard [37], and an insertion phase of the Line standards between 20 and 160 degrees, therefore it would need several Line standards for bandwidths larger than 8:1. However, several Line standards can also be used in smaller bandwidths to improve the accuracy of this calibration method [41].

- Line-Reflect-Match (LRM): it is similar to TRL calibration but substitutes the Through for a Match, which can be seen as an infinitely long transmission Line. Since it doesn't require several Line standards of different lengths, it is suitable for lower frequencies, as different electrical lengths might require too large physical length difference in measurement setups, and resistors have lower tolerances.

Since coupling effects from neighbouring devices can exist when measuring on-wafer [42], the accuracy of an on-wafer calibration can be increased by designing the calibration standards with similar surrounding environment [43]. This should create a similar coupling behaviour which could then be

de-embedded by the calibration algorithm. Naturally, the measured devices must have the same neighbouring environment as the calibration standards.

2.4 Wave propagation in guiding structures

A transmission line is a wave-guiding structure consisting of at least two conductors which have a constant section perpendicular to the propagation direction. Having two conductors enables the propagation of transverse electromagnetic (TEM) modes, with no cut-off frequency. The transmission line model [44] (see Fig. 2.1), uses shunt elements to describe the propagation of a single propagating mode through a differential electrical length.

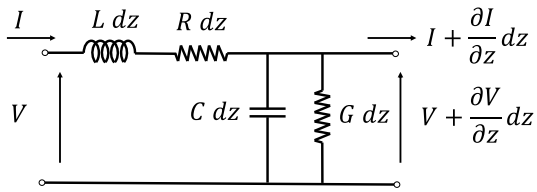

Figure 2.1: Equivalent circuit of a transmission line with a differential length.

The transmission line model has a series inductor, $L\,dz$, to account for the magnetic field around the conductors, and a shunt capacitance, $C\,dz$, to account for the displacement current flowing from the upper to the lower conductor. The series resistance, $R\,dz$, models the conductor losses whereas the shunt conductance, $G\,dz$, models the dielectric loss. The propagation constant, γ, and the characteristic impedance, Z_c, are then given by:

$$\begin{aligned} \gamma &= \sqrt{(R + j\omega L)(G + j\omega C)} = \alpha + j\beta \\ Z_c &= \sqrt{\frac{R + j\omega L}{G + j\omega C}} \end{aligned} \tag{2.15}$$

where γ describes how the magnitude and phase changes per unit length, whereas Z_c is the voltage-to-current ratio. Then, the voltage and current waves traveling in the positive and negative direction of a one-dimensional

space are:

$$V(z) = V^{+}e^{-\gamma z} + V^{-}e^{\gamma z}$$
$$I(z) = \frac{1}{Z_c}(V^{+}e^{-\gamma z} - V^{-}e^{\gamma z}) \tag{2.16}$$

2.5 Planar transmission lines

Some common planar transmission lines used at THz frequencies include:

- Parallel-plate waveguide (Fig. 2.2.a): it consists of two infinite long conducting planes sandwiching a dielectric material. Since it has a homogeneous dielectric, a pure TEM mode can propagate inside of it without dispersion.

- Coplanar waveguide (CPW) (Fig. 2.2.b): it consists of three metal strips with a ground-signal-ground configuration on top of a dielectric substrate. This transmission line has wide-band characteristics, negligible dispersion, manageable losses at THz frequencies, high sensitivity to its near-field environment, and provides easy interfacing with ground-signal-ground probes. Its main propagation mode is the even mode, taking its name from its even symmetry around the stripline, which is a quasi-TEM mode.

- Microstrip (Fig. 2.2.c): it consists of a finite width conducting strip and a conducting plane sandwiching a dielectric material, where most of the field lies between the two conductors. When the dielectric substrate is electrically small, the microstrip's propagating mode can be considered quasi-TEM with a certain effective permittivity. However, the inhomogeneous environment of the microstrip makes its a dispersive transmission line.

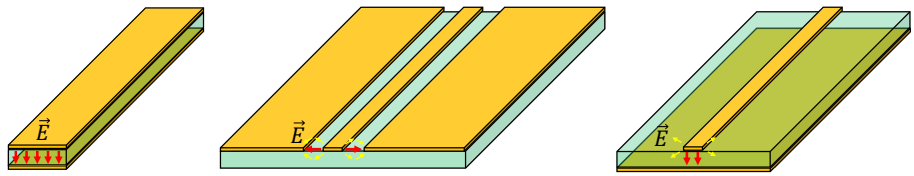

Figure 2.2: Sketches of the planar transmission lines **(a)** parallel-plate waveguide, **(b)** coplanar waveguide, and **(c)** microstrip, depicting the electric field of their main propagation mode. Orange color is used to depict conductors, whereas green represents dielectrics.

2.6 Single-wire waveguides

As well as single conductor hollow waveguides can propagate non-TEM modes above a certain cut-off frequency, a single solid conducting wire can propagate transverse magnetic (TM) modes as surface waves as long as the conductor has finite conductivity or it is in contact with a material with a higher dielectric constant than the surrounding environment. The main single-wire waveguides are the Sommerfeld line, the Goubau line, and the planar Goubau line.

2.6.1 Sommerfeld line

In 1899 Sommerfeld wrote a paper describing how a single conducting wire could propagate electromagnetic waves [45]. These TM propagating waves are symmetrical around the axis of the wire and have an electric field which spreads radially from the metallic wire (Fig. 2.3.a). Sommerfeld's wire had the peculiarity that it couldn't propagate electromagnetic waves if the metallic wire was perfectly conducting since the higher the conductivity the larger the extension of the field; thus if the wire is perfectly conducting, the field of a wave with finite amplitude would theoretically extend to infinity. Despite needing to limit the conductivity of the wire for allowing the propagation of waves, Sommerfeld's line had low loss propagation; however, it was never widely used since its extensive field could be easily affected by nearby objects.

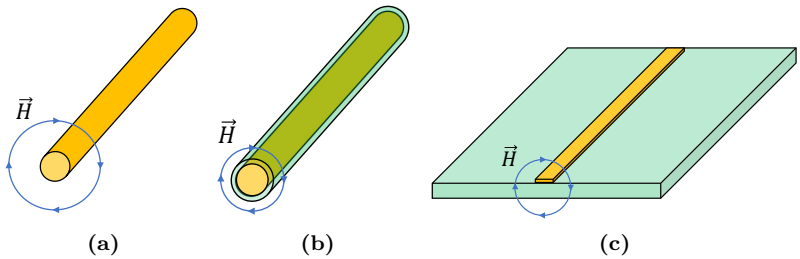

Figure 2.3: Sketches of the single-conductor waveguides **(a)** Sommerfeld line, **(b)** Goubau line, and **(c)** planar Goubau line, depicting their TM propagating mode. Note that field is more confined in the Goubau line than in the Sommerfeld line. In the planar Goubau line the field intensity is slightly more confined below the substrate. Orange color is used to depict conductors, whereas green represents dielectrics.

2.6.2 Goubau line

To increase the confinement of waves propagating in wires, Harms considered adding a dielectric layer to the wire [46], and the idea was further studied in detail by Goubau [47], [48]. The higher confinement of the field in this dielectric-coated wire (Fig. 2.3.b), now commonly referred as *Goubau line*, allows it to propagate waves even when a perfectly conducting wire is used and makes it less susceptible to suffer radiation loss from bends in the waveguide, compared to Sommerfeld's line. To excite the propagating surface wave [49] on both Sommerfeld's and Goubau's waveguide from a two-conductor transmission line, it is necessary to have a metallic conical structure to launch the propagation mode into the single conductor waveguides [48] (see Fig. 2.4.b) which ideally imposes the same field distribution of the propagating mode around the single conducting waveguide. This means that the larger the extension of the field of the single conducting wire, the larger the conical launching structure needs to be. By adding the dielectric layer to Sommerfeld's waveguide, Goubau increased the field confinement around the single conductor waveguide, making launching structures smaller.

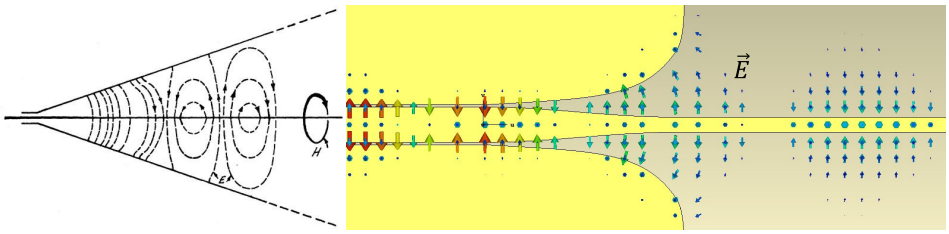

Figure 2.4: Mode-launching structures of **(a)** Goubau line, as depicted in [48], and **(b)** planar Goubau line. The TEM mode is progressively converter into a TM mode, which characterises the surface waves of this type of waveguides.

2.6.3 Planar Goubau line

Recently, Goubau's and Sommerfeld's lines have been used at THz frequencies showing low propagation loss [50], [51]. The low-loss and ultra-wide bandwidth performance of single conducting waveguides impulsed the development of a planar version of the Goubau line [52], consisting of a metallic strip deposited on top of a dielectric substrate (Fig. 2.3.c), which also has low loss and wide-band characteristics. Similarly to Goubau's and Sommerfeld's waveguide, the Planar Goubau Line (PGL) would need a launching structure if excited from a CPW [53] (see Fig. 2.4.b), which could be seen as the planar version of the metallic conical launching structure of Goubau's and Sommerfeld's waveguide. The PGL launcher starts as a three-conductor CPW [54], and progressively separates the lateral ground strips to smoothly transform, to avoid reflections and increase efficiency, the coplanar waveguide's propagating even-mode to the PGL's propagating mode.

The PGL has been used for sensing [53], [55] for its low loss characteristics, negligible dispersion, wideband operation, good liquid sample deposition and large field extension, which allows it to sense larger volumes. However, these planar waveguides have never been used for sensing around 1 THz using vector network analysers due to a lack of available technology until recently.

2.7 Substrate modes

When the electric size of the substrate thickness becomes comparable to the wavelength, the main propagating mode can leak its power to other radiating and parasitic modes in the substrate, increasing losses and causing undesirable resonances.

When the propagating mode in a CPW has an effective refractive index, n_p, higher than the refractive index in the substrate, n_s, it will produce radiating losses from the propagating mode in the CPW to the substrate. It will radiate in the direction where both modes have the same propagation constant in the direction of propagation of the CPW, forming a radiation semi-cone with angle θ_r given by [56]:

$$\cos\theta_c = n_p/n_s \tag{2.17}$$

and the attenuation constant, α_r, from radiation losses from a CPW is given by:

$$\alpha_r = \left(\frac{\pi}{2}\right)^5 \frac{(1-1/n_s^2)^2}{\sqrt{2(1+1/n_s^2)}} \frac{(s+2w)^2}{K(k)K'(k)} \tag{2.18}$$

where α_r is given in Neper per metre, s is the CPW's central strip width, w is the CPW's gap width, $k = s/(s+2w)$, and K and K' are the complete elliptic integrals of the first and second kind, respectively.

When the substrate's thickness, d, is in the order of a wavelength, one must take into account the reflections of the substrate-air interface [57]. A CPW without back-side ground-plane, it can be seen as a semi-grounded dielectric slab which will have surface waves similar to the odd TE and even TM modes of an ungrounded dielectric slab of twice the thickness [58], or a Zenneck wave [49]. The cut-off frequency of these surface modes are given by [59]:

$$\begin{aligned} \text{For TE}_m \text{ modes:} \quad & f_c = \frac{m}{4d}\frac{c}{\sqrt{n_s^2-1}} \quad \text{where } m = 1,3,... \\ \text{For TM}_m \text{ modes:} \quad & f_c = \frac{m}{4d}\frac{c}{\sqrt{n_s^2-1}} \quad \text{where } m = 0,2,... \end{aligned} \tag{2.19}$$

The interaction of the propagating wave with these surface waves depends on the overlap of their field distributions and if the phase velocity of the propagating mode is similar or higher than that of the surface wave, causing dispersion and radiation losses. This phenomenon is similar to what happens

in an optical fibre, where the light will leak from the core if the refractive index of the cladding is higher than in the core. At the frequency where the phase velocity of the two waves is equal, the dispersion will be maximum, whereas the leakage losses are proportional to frequency. To minimise these undesirable effects, the cut-off frequency of all modes except for the TM_0 mode (with no cut-off frequency) can be increased by choosing an electrically thin substrate. A conservative rule-of-thumb is given in [57], where the substrate thickness is suggested to be taken as:

$$d < 0.12\lambda_0/n_s \tag{2.20}$$

Other suggested methods for reducing radiation losses in CPWs [60] include narrowing CPW conductors ($\lesssim \lambda/30$), although conductor losses become too high at THz frequencies; adding a superstrate on top of the CPW, which would decrease the phase velocity, decreasing or stopping radiation losses to the substrate.

If the CPW doesn't have a large ground-plane, a TE_0 surface mode can propagate in the ground-less part of the substrate [61], increasing the possibilities for different types of parasitic mode excitation. For the case of a PGL, its propagating mode is essentially the same TM_0 mode as the surface wave with the lowest cut-off frequency in a CPW with a large ground plane. The difference lies in that the PGL mode propagates both above and below the substrate, whereas the undesirable TM_0 surface wave in the CPW propagates only below the substrate. The PGL might not have to deal with the TM_0 surface wave, but as the CPW without a large ground-plane, it could excite TE_0 in the parts of the substrate without a conductor. Added to this, since the PGL field concentrates in the edges of the conducting strip, the field distribution will overlap to that of the TE_0 mode, increasing their interaction. In general, the cut-off frequency of the surface waves that can propagate in a ground-less dielectric slab are given by [59]:

$$\begin{aligned} &\text{For } TE_m \text{ modes:} \quad f_c = \frac{m}{2d}\frac{c}{\sqrt{n_s^2 - 1}} \quad \text{where } m = 1, 2, ... \\ &\text{For } TM_m \text{ modes:} \quad f_c = \frac{m}{2d}\frac{c}{\sqrt{n_s^2 - 1}} \quad \text{where } m = 1, 2, ... \end{aligned} \tag{2.21}$$

2.8 Permittivity Extraction from S-parameters

When measuring a sample contained in a device it can be desirable to de-embed part of the device from the measurements with a two-tier calibration [20], obtaining measurements focused on the sample being measured.

A simple de-embedding technique can be done by measuring a known sample together with the sample under test in the same setup. Considering a reference sample with known refractive index, $\hat{n}_r$, the effective refractive index of the line with sample, $\hat{n}_e$, can be calculated using:

$$\hat{n}_e = \hat{n}_r - \frac{\ln\left[S_{21}^{(s)}/S_{21}^{(r)}\right]}{jk_0 l_s} \tag{2.22}$$

where $S_{21}^{(s)}$ and $S_{21}^{(r)}$ are the complex transmission coefficient for sample and reference respectively, k_0 is the vacuum wavenumber, and l_s is the effective length of the sample. This method is a robust method requiring only a transmission or reflection measurement.

A more complex two-tier calibration method was developed by Bao et al. [62], which de-embeds transmission lines with samples on top with different line lengths, using full S-parameter measurements. It is based on the assumption that a dielectric material on top of a planar waveguide only changes the capacitance, C, and conductance, G, of the transmission line parameters, in eq. (2.15), it can relate the reference and sample S-parameter results to a change in the tested sample. Combining equation (2) in [62] together with the relation $\gamma = jk_0\hat{n}$, yields the following equation:

$$\begin{aligned}\mathrm{Tr}\{[T_e]\cdot[T_r]^{-1}\} = {} & 2\cos(k_0 l_r n_r)\cos(k_0 l_e n_e) + \\ & + \left(\frac{n_r}{n_e} + \frac{n_e}{n_r}\right)\sin(k_0 l_r n_r)\sin(k_0 l_e n_e)\end{aligned} \tag{2.23}$$

where l is the physical length of the transmission line section containing the sample, k_0 is the vacuum wavenumber, and n_r and n_e are the effective complex permittivities of the reference and sample-loaded transmission lines, respectively. $[T_r]$ and $[T_e]$ are the transfer scattering matrices of the reference and sample-loaded transmission line, respectively, which can be directly obtain from the measured S-parameters [63]:

$$[T] = \begin{pmatrix} \frac{1}{S_{21}} & \frac{-S_{22}}{S_{21}} \\ \frac{S_{11}}{S_{21}} & \frac{(S_{12}S_{21}-S_{11}S_{22})}{S_{21}} \end{pmatrix}$$

This method has the advantage that it uses both transmission and reflection measurements of a reference and a sample measurement to characterise the sample permittivity. However, due to this it also makes it a less robust technique.

CHAPTER 3

Method

This chapter explains how devices and their calibration standards were designed and fabricated in our in-house cleanroom (Section 3.3). Later, it describes the design and fabrication of the microfluidic channel, (Section 3.4), the measurement setup (Section 3.5), and the sample characterisation method (Section 3.6).

3.1 Simulations

In this thesis, electromagnetic simulations have been used for the design of the CPW and PGL structures, and to verify measurements. Simulations were done in CST Studio Suite.

3.1.1 Simulation of PGL port

The possibility of exciting the PGL directly, without needing an intermediate mode transformer, would reduce simulation time and provide a better

simulation environment for future analysis/synthesis of PGL elements.

The simulated PGL was excited with a square wave port centred around its conducting strip. Since the wave port has perfect conducting edges, the excited mode is similar to a square coaxial-line mode. In [48] Goubau explains how a coaxial with an inner conductor coated in dielectric causes the field to have a longitudinal electric component. If the outer conductor radius of the coaxial is increased, there is a point where it no longer changes the field distribution around the inner conductor. As a consequence, the characteristic impedance's value of the dielectric-coated coaxial saturates after a certain outer conductor radius, unlike the uncoated coaxial's impedance which continues to increase logarithmically (Fig. 3.1.a). Since the PGL has a similar TM mode to the Goubau line, these results suggest that for a sufficiently large wave port both the S-parameter results and the impedance value should converge. Indeed, simulation results (Fig. 3.1.b) show that the port impedance saturated for increasing port size, similarly to Goubau's results. Similarly, S-parameter results also converged for increasing port size (Fig. 3.2). Thus the port size was taken as the smallest size which yielded convergent simulated S-parameter results, with 800 µm sides in a square wave-port.

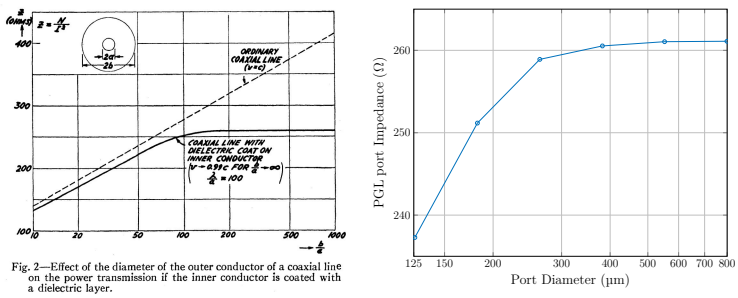

Fig. 2—Effect of the diameter of the outer conductor of a coaxial line on the power transmission if the inner conductor is coated with a dielectric layer.

(a) **(b)**

Figure 3.1: Simulated PGL port impedance is coherent with theory. (a) Figure taken from [48] depicting the impedance of coaxial with dielectric coating in inner conductor. **(b)** Simulated PGL port impedance vs. square port size, showing similar behaviour as Goubau's results.

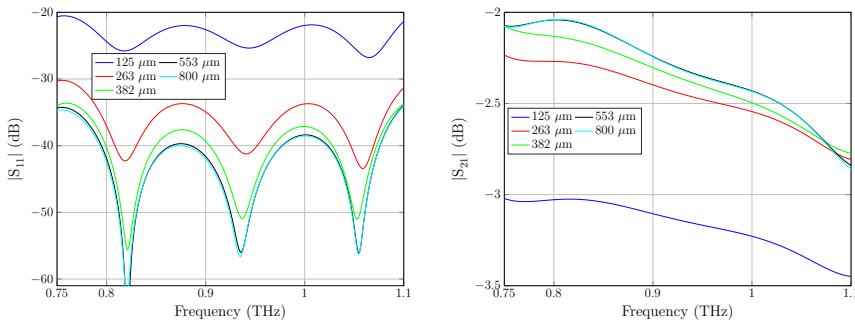

(a) **(b)**

Figure 3.2: Simulation results using PGL port converge for sufficiently large PGL port size. CST simulation results of **(a)** S_{11} and **(b)** S_{21} of a 3 mm long PGL for different port sizes.

3.2 Design of the planar waveguides

When sensing liquids samples with planar waveguides, the sensitivity increases if the field is in contact with the sample and if their propagation losses are minimised, which increases the SNR of the measurement. In this thesis, we have considered two types of planar waveguides which have their maximum field intensity on top of the substrate: CPW and PGL which have been designed to minimise their losses.

3.2.1 Coplanar waveguide

CPWs were designed to have low losses and to be suitable for probing with ground-signal-ground 25 µm pitch probes [21]. The main design parameters of the CPW are its strip-, gap-, and ground plane width, and the substrate's material and thickness. The strip, s, and gap, w, widths were designed to have the centre of the CPW gaps between the centre of the probe tips, for better probing, following the equation $s + w = 25$ µm. Additionally, the CPW was designed to have the same characteristic impedance as the probe, 50 Ω, minimising reflections. Ground planes were chosen to be electrically big to avoid parasitic effects.

Regarding the substrate, it was chosen to be as thin as possible and from a low dielectric material, to avoid substrate modes, as seen in section 2.7. Plastics usually have very low losses at THz frequencies [64] and have a low dielectric constant, which makes them ideal for having a low-loss and electrically thin substrate. Some plastics cannot handle high temperatures (100 °C) required in the fabrication process, so we chose a plastic with good electrical properties while having a relatively high melting point and having mechanical strength. Considering this, a 23 µm polyethylene terephthalate film (Mylar® A, fabricated by DuPont) was chosen as substrate, with a relative permittivity of $\epsilon' = 3.15$ and $\tan(\delta) = 0.017$ at 1 THz [64].

Additionally, multi-Line TRL calibration standards were designed for CPW and fabricated integrated into the devices' chip. The Trough standard has a total length of 210 µm, placing the calibration plane at its mid-point, 105 µm from the start of the CPW. The Line standards were designed with electrical lengths of $\lambda/4$, $3\lambda/4$, and $11\lambda/4$ at the centre of the measured band, 910 GHz.

3.2.2 Planar Goubau line

The design of a PGL involves few degrees of freedom, mainly: strip width, and choosing the substrate permittivity and thickness. Simulation results indicated that the PGL losses were most sensitive to the substrate material and thickness since it would increase radiation losses into other modes [60]. Thus, as for the CPW, the substrate was chosen as an ultra-thin 23 µm thick PET film, which should minimise losses from coupling to other modes.

The PGL can be excited with ground-signal-ground probes using a CPW-to-PGL mode converter. The probes contact the CPW section in the converter, exciting the CPW's quasi-TEM even mode, which is then converted into the PGL's TM mode. This mode converter progressively separates the lateral ground planes of the CPW, until the propagating mode is confined exclusively on the central strip, thus becoming a PGL (Fig. 3.3).

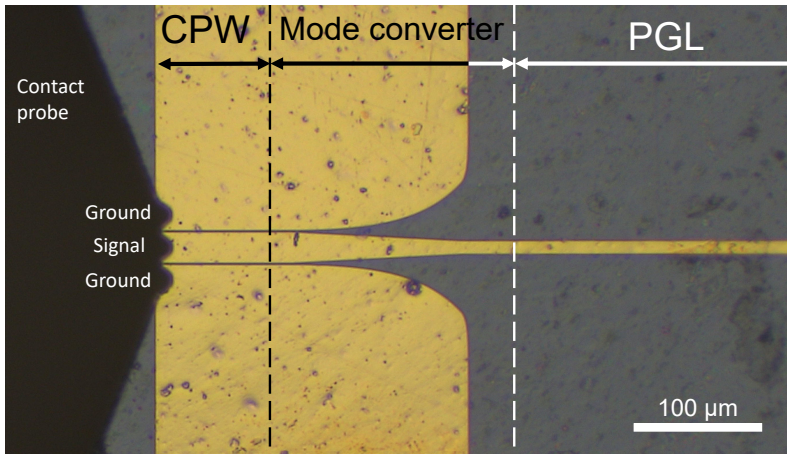

Figure 3.3: The CPW-to-PGL mode converter can be used to excite a PGL with ground-signal-ground probes. Micrograph of the ground-signal-ground probe contacting the CPW mode converter.

For designing a low-loss CPW-to-PGL mode converter, (1) the impedance changed geometrically, to minimise reflections, (2) avoided small CPW strip and gap dimensions, which would increase conductor losses, (3) used the length which minimised the insertion losses, as a too-short converter would have high reflections, and a too-long converter would add unnecessary line losses.

3.2.3 Planar Goubau line calibration standards

In this thesis, calibration standards were developed for planar Goubau lines for the first time, using multi-line TRL calibration. Three Lines standards were designed with electrical lengths of $\lambda/4$, $3\lambda/4$ and $11\lambda/4$ at the geometrical centre frequency of the band, at 910 GHz. For the Reflect calibration standard, a highly reflective element needs to be designed. Several designs of Reflect standards were tested using electromagnetic simulations. The best performance was achieved by a T-shaped structure terminating the planar Goubau line (Fig. 3.4.a) with a span of $\lambda/2$. The Reflect standard has a maximum electric field intensity at the ends of the T-sidearms (Fig. 3.4.b), creating a null of electric field intensity in the intersection, thus the structure behaves as a short-circuit at the intersection point of the T-shaped structure.

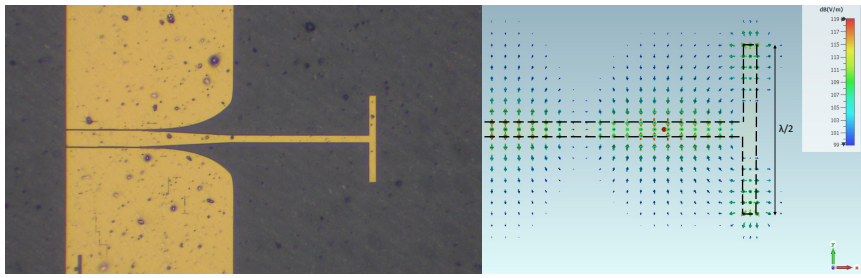

(a) **(b)**

Figure 3.4: Layout of PGL Reflect standard. **(a)** Micrograph of one of the fabricated PGL Reflect standard. **(b)** Electric-field distribution around the PGL Reflect standard, showing a minima at the intersection of the Tee. Dashed lines are used to help visualise the perimeter of the Reflect standard.

3.3 Device fabrication

The CPWs and PGLs with their corresponding dedicated calibration standards were fabricated in our in-house cleanroom using electron-beam lithography and evaporation of 20 nm Ti and 350 nm Au on top of the PET substrate. The fabrication was done according to the following steps, represented in Fig. 3.5:

1. Mount the 23 µm thick PET film on low resistivity 2-inch silicon wafers using thin film wax.

2. Spin electron-beam lithography resist and auxiliary layers:
   a) Spin HMDS (negligible thickness) at 3000 rpm for 30 s. Acceleration time: 1 s. No baking.
   b) Spin MMA 8.5 EL10 (450 nm thick) at 3000 rpm for 30 s. Acceleration time: 1 s. Bake in oven for 10 min at 110 °C. Spin PMMA A2 (70 nm thick) at 3000 rpm for 30 s. Acceleration time: 1 s. Bake in oven for 10 min at 110 °C.
   c) Spin Espacer 300Z (20 nm thick) at 1500 rpm for 60 s. Acceleration time: 1 s. Bake on hot plate for 90 s at 80 °C.

3. e-beam lithography (current 30 nA, dose 320 µC/cm^2).

4. Substrate development:

   a) Developed in IPA:DI-H_2O in 10:1 volume ratio for 40 seconds.

   b) Ash O_2 plasma for 5 s at 40 W.

5. Deposited Ti/Au 200/3500 Å.

6. Lift-off in 65 °C acetone.

7. Detach the PET film from the silicon wafer

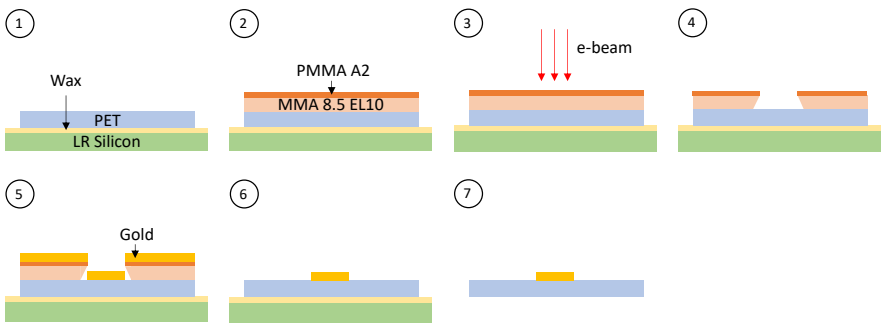

Figure 3.5: Sketch of the fabrication steps. Figure is not to scale

3.4 Microfluidic channel

Microfluidic channels offer a good solution for guiding liquid samples into the sensing area of a chip, also giving control of the shape of the sample with micrometre precision, and avoiding its evaporation. The microfluidic channels used in this thesis were fabricated in polydimethylsiloxane (PDMS), with a square cross-section channel. The channel's cross-section was designed to have 100 µm sides and had a fabricated side of 123 µm. The width of the microfluidic channel was measured with an optical microscope capable of measuring dimensions with a resolution of 1 µm.

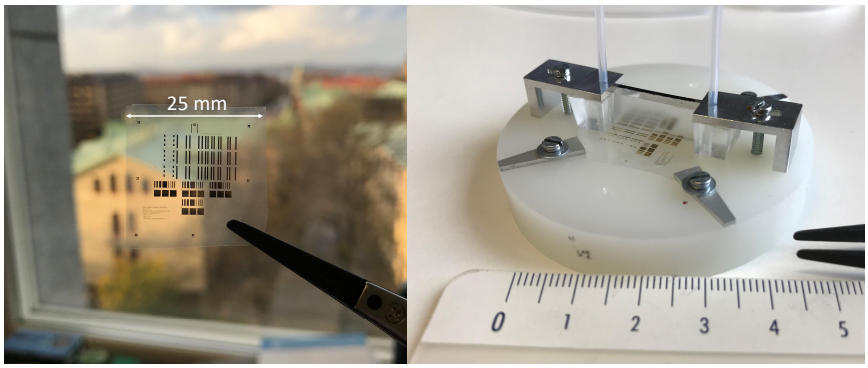

(a) **(b)**

Figure 3.6: **(a)** Photograph of the fabricated chip. **(b)** Photograph showing the PET chip with devices which is held on to the PE supporting substrate. The PDMS with the microfluidic channels is clamped to the supporting substrate and in remains in contact with the devices.

The PDMS microfluidic channel was fabricated as follows:

1. Mix PDMS with the curing agent (cross-linker) with a 10:1 ratio.
2. Stir the mixture thoroughly in a container, so it becomes homogeneous.
3. De-gas the PDMS
   a) Put the container with the PDMS inside a vacuum bell.
   b) Generate vacuum. If there is too much PDMS, the foam might overflow, so release vacuum to avoid that.
   c) Repeat process of generating and releasing the vacuum to get rid of bubbles in the PDMS.
4. Put the PDMS in the mould to give the desired shape. Repeat de-gassing step.
5. Cure the PDMS in the oven at 60 °C for 12 hours. The mould used for shaping the PDMS is made of PMMA, which should avoid temperatures higher than 60 °C.

The PDMS with the microfluidic channel was attached to the DUT by using a metal clamp which tightened the PDMS to the supporting substrate (Fig. 3.6.b). The clamping was done under the microscope to align the microfluidic channel to the DUT.

3.5 Measurement setup

The devices were characterised measuring 2-port S-parameters. Fig. 3.7.a shows a sketch of the measurement setup including:

- **Vector Network analyser (VNA):** model Keysight N5242A (10 MHz to 26.5 GHz) setting up an IF bandwidth of 50 Hz for achieving a low noise floor.
- **Frequency extenders:** when measuring S-parameters at THz frequencies, signal multipliers are used to convert the VNA's signal into a higher frequency signal, covering the band which needs to be measured. The process of frequency conversion comes at the price of a conversion loss, which increases with the multiplication factor. The multiplication factors used in this case are 81 and 72 for RF and LO signals respectively and achieved frequencies from 0.75 THz to 1.1 THz. The frequency extenders used were VDI WR1.0SAX, with a typical/minimum dynamic range of 69 dB and 50 dB.
- **External RF and LO sources:** used instead of the internal VNA sources to achieve a higher dynamic range (about 5 dB gain) in the measurements thanks to their ultra-low phase noise characteristics. When using multipliers to achieve higher frequencies, the phase noise deteriorates, and thus strict specifications on phase noise have to be imposed on the sources at this frequency band. The external sources used were Keysight E8257D (250 KHz to 20 GHz). The RF and LO output power were set to 7 dBm and -4 dBm respectively.
- **Ground-Signal-Ground (GSG) Probes**: used as the interface between the frequency extenders and the DUT (3.7.b), the probes convert the rectangular waveguide from the extenders to a CPW line which terminates in the GSG tips which are used to couple the field into the structures to be measured. Cascade's T-Wave probes [21] were used for

measuring between 0.75 THz and 1.1 THz (WR 1.0 band) and have a probe pitch of 25 µm.

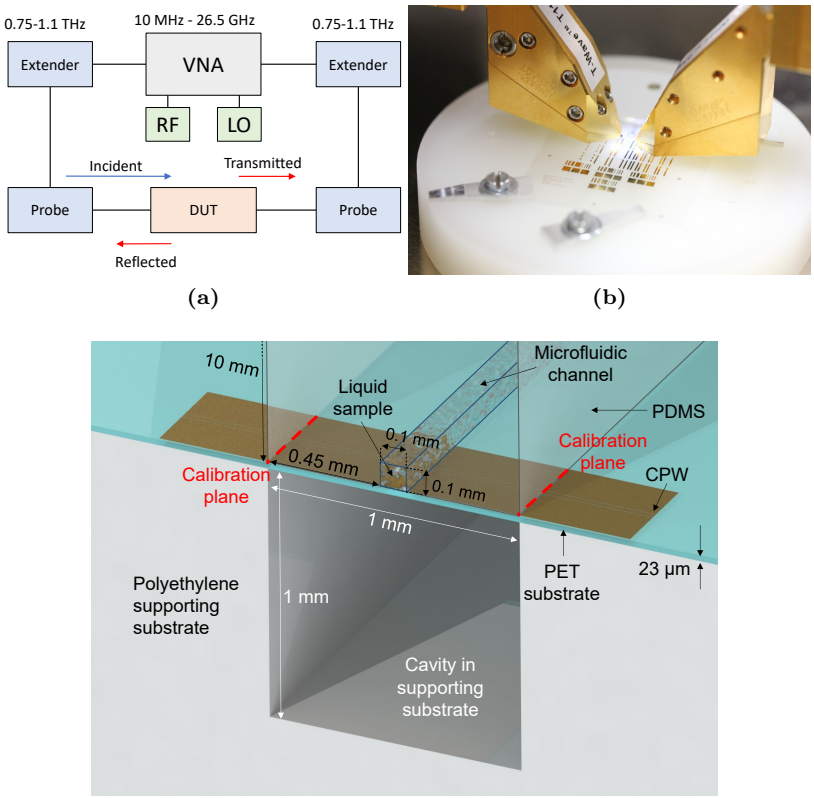

Figure 3.7: (a) Sketch of on-wafer S-parameter measurements setup. (b) Probes measuring the devices without the microfluidic channel. (c) Sketch of the CPW when being measured with the microfluidic channel and samples. Probes contact the CPW at the edge of its sides.

A supporting substrate, immediately below the device substrate, is necessary when measuring to avoid having the ultra-thin PET film with the devices on top of the metal chuck of the probe-station, which would affect the

propagation mode of the PGL, likely becoming a microstrip due to the new conducting plane. However, since the PGL's field distribution has a larger extension, its propensity to radiate will be also affected by other surrounding materials, such as the supporting substrate. Thus, the supporting substrate will have to have a lower dielectric material than the device's substrate to decrease its refractive index, to avoid leakage from the PGL's propagating mode, according to [60]. The supporting substrate was chosen as a 6 cm in diameter and 1 cm thick polyethylene (PE) cylinder, with a relative permittivity of ϵ_r = 2.3 and a loss tangent of $\tan(\delta)$ = 0.004. The chip was clamped on to the supporting substrate to avoid any movement during measurements. The supporting substrate has a 1 mm deep and 1 mm wide hole which is aligned with the measured devices to avoid radiation losses (Fig. 3.7.c).

The sample was delivered to the microfluidic channel using a manually operated syringe with tubings which connected to the PDMS microfluidic channels.

3.6 Sample characterisation

The sample permittivity was obtained from the measured transmission parameters, S_{21}, using the CPW as sensing structure. The diagram in Fig. 3.8 offers an overview on the process, which consists of two main steps: (1) obtaining the effective refractive index of the CPW loaded with the sample, and (2) translating this effective refractive index into the sample's refractive index.

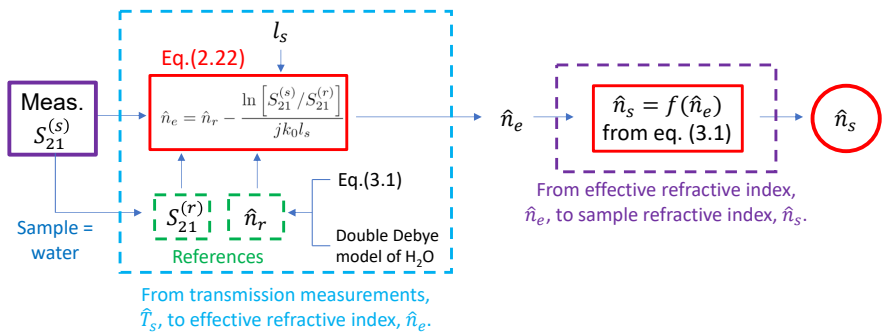

Figure 3.8: Diagram showing how the sample's refractive index was obtained from the transmission measurements.

The calibrated measurements in our setup have the calibration plane in the interface between the air and the PDMS (see red discontinuous line in Fig. 3.9). However, for characterising the sample, we move the measurement plane to the PDMS-liquid interface (discontinuous yellow line in Fig. 3.9). For this, we used eq. (2.22) with sample measurements, information of the sample length and a known reference measurement, with water as a sample.

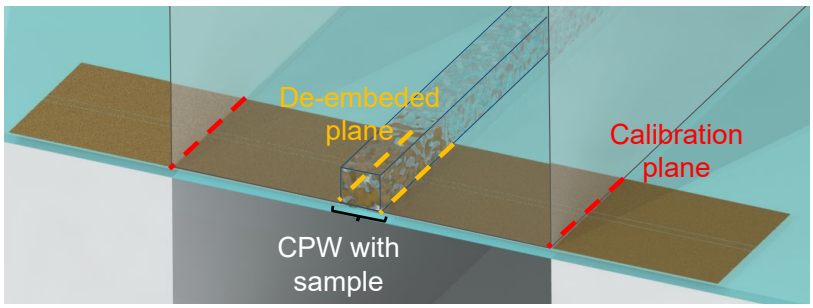

Figure 3.9: The de-embeding techniques allow to move the measurement plane from the calibration plane to the region where the sample lies.

The reference effective refractive index, $\hat{n}_r$, for the CPW was obtained using an analytical expression for multi-layered CPWs [65] together with a double Debye model of water [14]. Water is a sample which has been studied extensively at THz frequencies and thus has accurate material properties at THz frequencies.

In [66] a more complex method is proposed for obtaining the propagation constant of a line with a sample, based on measurements of a reference line, using full S-parameter measurements. However, this method could not be implemented for our measurements since the reflection parameters, S_{11} and S_{22}, showed to be very sensitive to probing conditions.

After calculating the effective refractive index of the CPW containing the sample, with eq. (2.22), we calculated the sample's permittivity. For it, we used an analytical expression for multi-layered CPWs [65], which relates the effective refractive index of the CPW with the sample permittivity according

to the equation:

$$\hat{n}_e^2 = \hat{\epsilon}_e = 1 + \frac{1}{2}(\hat{n}_s^2 - 1)\frac{K(k)K(k_s')}{K(k')K(k_s)} + \\ + \frac{1}{2}(\hat{n}_{sub}^2 - 1)\frac{K(k)K(k_{sub}')}{K(k')K(k_{sub})} \tag{3.1}$$

where the operator K is the complete elliptical integral of the first kind, and k, k', k_s, k_s', k_{sub}, k_{sub}', depend on the geometry of the CPW cross-section, superstrate and substrate, respectively [65]. This analytical expression agrees with simulation results of a multi-layered CPW.

CHAPTER 4

Results

This section shows measurements validating the PGL calibration standards, a comparison between PGL and CPW losses from 750 GHz to 1100 GHz, and the use of CPWs and PGLs integrated with microfluidic channels for using them as a THz spectroscopy sensor.

4.1 PGL calibration standards

Designing the Through and Line standards for a PGL TRL calibration is trivial, and their frequency response should be predictable. On the other hand, the designed Reflect standard has a more complex field distribution, so its design must be validated in both simulations and measurements. Fig.4.1 shows the good agreement between simulations and measurements of the designed and fabricated Reflect standard. Simulated S_{21} is lower than -95 dB in all the band, whereas the measured S_{21} lies at the noise-floor level, around -35 dB. The calibration plane is marked with a red discontinuous line in the inset of the figure and is located 105 µm inside the CPW.

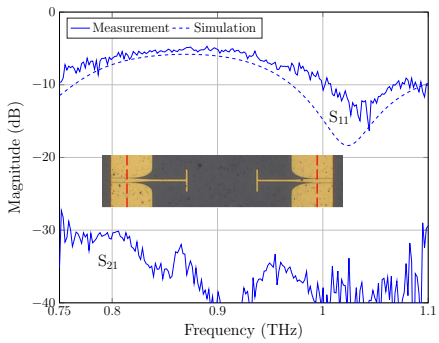

Figure 4.1: Simulations and measurements of the PGL Reflect have good agreement when using a established TRL CPW calibration. S-parameter comparison of simulations (dashed line) and measurements (solid line) of the Reflect standard. Simulated S_{21} is lower than $-95\,\mathrm{dB}$ in all the band, and does not appear on the figure. Inset shows a micrograph of the PGL Reflect, with the calibration plane of the simulation and measurements depicted as a dashed line, set $105\,\mu\mathrm{m}$ into the CPW line.

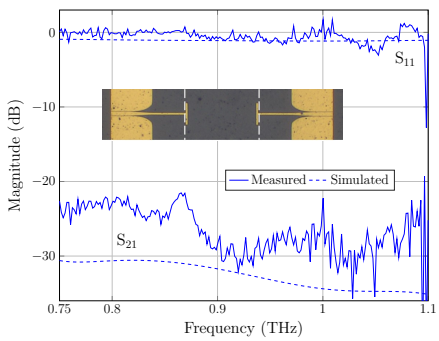

Figure 4.2: Simulations and measurements of the PGL Reflect have good agreement when using the proposed PGL TRL calibration. S-parameter comparison of simulations (dashed line) and measurements (solid line) of the PGL Reflect standard. Inset shows a micrograph of the PGL Reflect, with the calibration plane of the simulation and measurements depicted as a dashed line, set after the CPW-to-PGL mode converter, along the PGL.

The Reflect was measured after calibrating measurements with the proposed multi-line TRL calibration standards, which sets the calibration plane after the CPW-to-PGL mode converter (see discontinue line in the inset of Fig. 4.2). The Reflect measured was different from the one used for the calibration. The S-parameter measurement results of the PGL Reflect show to have high and wideband reflection characteristics, with over $-1.1\,\mathrm{dB}$ in all the band (Fig. 4.2). The transmission measurements on the other hand show to be very low, as expected. Simulations using a PGL wave-port, showed to agree with the measurements results, having high reflectivity, and low transmission. The simulations results showed in Fig. 4.2 were obtained by exciting a PGL line terminated in the Reflect standard, and de-embedding the PGL line in the simulation software.

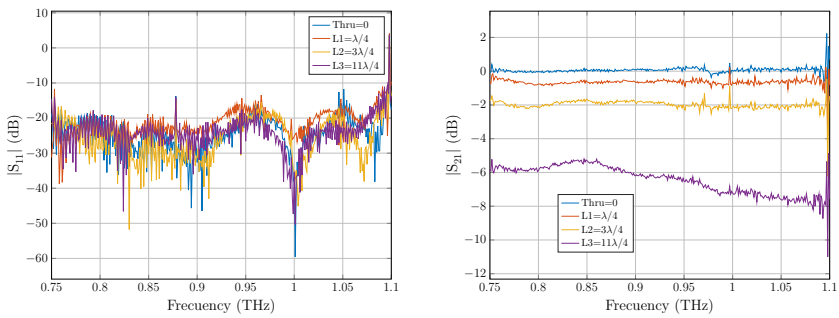

(a) **(b)**

Figure 4.3: Measurements of PGLs of different lengths after calibrating demonstrate good quality of calibration. Measured magnitude of **(a)** reflection (S_{11}) and **(b)** transmission (S_{21}) of the Through and multiple lines in the calibration standard. The low value of $|S_{11}|$ indicates a correct de-embedding of the CPW-PGL mode transformer, while the values of $|S_{21}|$ yield expected behaviour for lines at these frequencies.

In addition to the PGL Reflect, we also measured the PGL Through and Line standards, choosing structures which haven't been used during the calibration. In Fig. 4.3 we show the measured transmission and reflection of Through and Lines from the calibration standards after applying the PGL calibration. The low reflection and the smooth transmission indicate that

the calibration method has correctly de-embedded the CPW-to-PGL mode converter.

Fig. 4.4 shows the simulated and measured S-parameters for a 1 mm long PGL using the PGL TRL calibration. The results of the magnitude of the transmission, $|S_{21}|$, show to be flat except for a subtle decrease proportional to the frequency, for both measurements and simulations. The results for the phase of the transmission, show to have a steady response with frequency, indicating negligible dispersion in the PGL. There is a slight difference in the slope of the phase of the transmission between measurements and simulations, indicating that the substrate material (PET) might have a lower permittivity value than the one reported in literature [64]. The measured reflection parameter, S_{11}, shows to be typically below −10 dB, with higher values at the higher-frequency side of the band. Ideally, these values should be as low as possible, but the reflection coefficient is very susceptible to the probing conditions, making reflection measurements more unreliable than the transmission measurements.

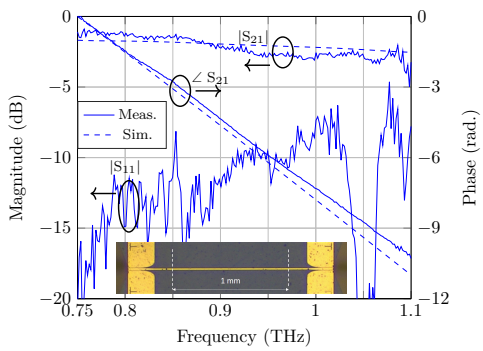

Figure 4.4: Simulations and measurements of a 1 mm long PGL using the proposed PGL TRL calibration. S-parameter comparison of simulations (dashed line) and measurements (solid line) of the PGL Reflect standard. Simulated S_{11} results are below −30 dB in all the band. Inset shows a micrograph of the PGL Reflect, with the calibration plane of the simulation and measurements depicted as a dashed line, set after the CPW-to-PGL mode converter, along the PGL.

At THz frequencies, even small changes in probing conditions can have a significant change in the reflection measurements, since the probe-substrate

interface well lies behind the calibration plane, making small reflections appear larger.

Overall the developed PGL calibration standards show to be able to set the calibration plane along the PGL, accurately de-embedding the CPW-to-PGL mode converter and probe-substrate transition.

4.2 Planar waveguide loss

At THz frequencies, the available power of electronic sources tends to be lower than at lower frequencies, and conductor and radiation losses tend to increase with frequency. Thus it is especially important to keep losses at minimum to have a higher dynamic range for measuring lossier devices and higher measurement SNR for being able to detect small signal changes.

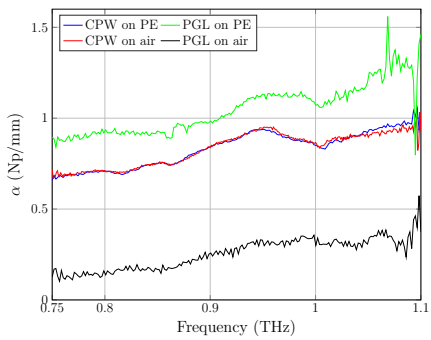

Figure 4.5: Attenuation coefficient measurements of a 1 mm long CPW and PGL. Measurements were done on two setups: placing the device on top of a PE supporting substrate or suspending it on air.

We compared S-parameter measurements of two planar metallic waveguides, the CPW and the PGL, fabricated with the same method depositing gold on an ultra-thin PET film substrate. For each waveguide, CPW or PGL, the measurements were calibrated using their own calibration standard included in the chip. Fig. 4.5 shows the attenuation coefficient measurements for the CPW and PGL done with and without a polyethene (PE) supporting substrate below the PET substrate. It can be seen that when using the PE supporting substrate, the CPW has lower losses than the PGL. However, when

the measured waveguides are suspended on air—by placing them on top of a micromachined hole in the PE supporting substrate—the losses of the PGL drop drastically, whereas the CPW losses remain unchanged. Without the supporting substrate, the PGL becomes a more power-efficient planar waveguide compared to the CPW, with an attenuation coefficient of 0.32 Np/mm at 1 THz. The main reason why the PGL reduces its radiation losses is that the PGL's field distribution is much wider, reaching the supporting substrate and causing radiation losses since the refractive index in the supporting substrate is higher than the effective refractive index of the PGL. In contrast to this, the CPW has a more confined field and the supporting substrate is electrically distant to make a significant impact on the losses.

4.3 Sensing of aqueous samples

We measured the magnitude and phase of the transmission of a 1 mm CPW having a microfluidic channel clamped on top which delivered aqueous samples (see Fig. 3.7.c). The aqueous samples consisted of propan-2-ol and deionized water (DI-H_2O) mixtures with volume concentrations between 50% and 100% DI-H_2O in steps of 10%. To obtain the sample refractive index from these transmission measurements, we followed the process shown in Fig. 3.8.

Fig. 4.6.a-b shows the relative S_{21} CPW measurements obtained for the different mixtures of water and propan-2-ol using pure DI-H_2O as reference. The solid lines represent the mean of five measurements collected in consecutive VNA frequency sweeps, whereas the shadowed area represents the standard deviation of the five measurements. Both the magnitude and phase measurements show to have sufficient SNR for distinguishing between samples despite the high losses of the aqueous samples, being magnitude measurements more sensitive to changes than phase measurements.

The effective refractive index results of the CPW with samples was calculated from the relative CPW transmission measurements using eq. (2.22). The resulting real and imaginary parts of the effective refractive index are plotted in Fig. 4.6.c-d.

Once the effective refractive index of the CPW with the sample has been obtained, the sample's refractive index was calculated by using eq. (3.1).

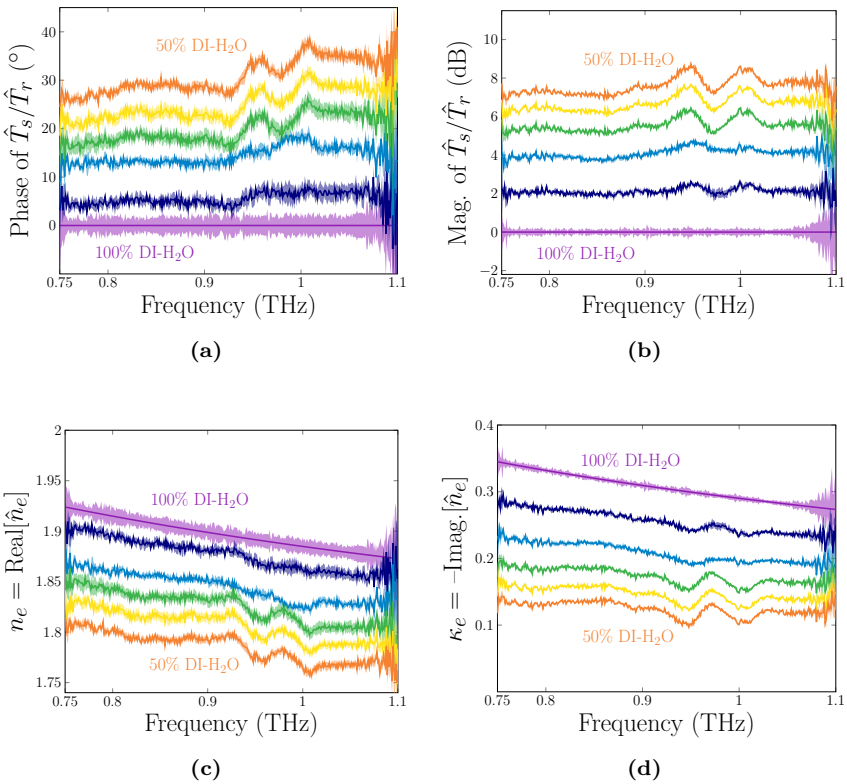

Figure 4.6: The sample gradient yields distinguishable magnitude and phase changes in the transmission. Measured **(a)** phase and **(b)** magnitude of the transmission, normalised with respect to the case of having pure water as sample. Extracted **(c)** real and **(d)** imaginary part of the effective refractive index of the CPW with sample, calculated using eq. (2.22). Samples consist of IPA/DI-H_2O mixtures with water volume concentration from 50% to 100% in steps of 10%. Measurements were performed five times in consecutive frequency sweeps. Solid line represents the mean, and the shadow represents the standard deviation of the measurements.

The sample's refractive index vs. water sample concentration is plotted in Fig. 4.7 for 0.8 THz, together with literature values of IPA/H_2O mixtures, and

the modified model for polar liquids, eq. (2.7), using a fitting factor of $a = 1.33$ for propanol samples [28]. The figure shows how our measurements show consistent change of real and imaginary permittivity vs. sample concentration, having small error bars, and being able to measure samples with high water content using an on-chip setup.

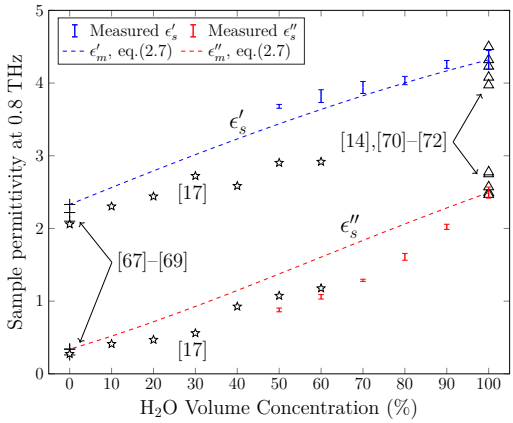

Figure 4.7: Measured permittivities show consistent change versus water concentration. Real and imaginary permittivity of IPA/DI-H_2O samples vs. water concentration at 0.8 THz for this work (blue and red errorbars with 95% confidence interval) and literature values. Literature values of (+) IPA [67]–[69], (△) water[14], [70]–[72], and (☆) IPA/H_2O mixtures measured with a similar on-chip method [17] are plotted. The dashed lines show the modified Bruggeman's model for polar liquids for the change in water concentration, based in eq. (2.7).

It is worth noting that the PDMS channel showed to swell by pure IPA, which reduced the microfluidic width to 113 µm. However, samples with an IPA concentration lower than 50% showed not to have any impact on the channel width. Similarly, propan-1-ol (with similar Hildebrand solubility parameter and dipolar moment as IPA) was reported to have a swelling factor of 9% in PDMS, whereas water produced no swelling [73].

The noise floor of the measurements gives an indication of the system's dynamic range. The noise floor was measured for two different calibration planes: (1) rectangular waveguide calibration (Short-Open-Load-Through),

at the interface between the frequency extenders and contact probes, and (2) CPW calibration, at the calibration plane used for measuring. The noise floor was measured from S_{21} when ports 1 and 2 were isolated, after applying each calibration. Fig. 4.8.a shows the values of the noise floor across frequency for each calibration, together with the SNR of the CPW measurements with water as a sample. The frequency-averaged dynamic range of the CPW calibration is −49 dB, for the rectangular waveguide calibration is −69 dB, and the frequency-averaged SNR of the CPW with water is 25 dB. The noise floor could be further improved by using time-averaging techniques.

Fig. 4.8.b shows the output power across frequency for the frequency extenders used to measure, having at least −44 dBm and −39 dBm of power for each extender.

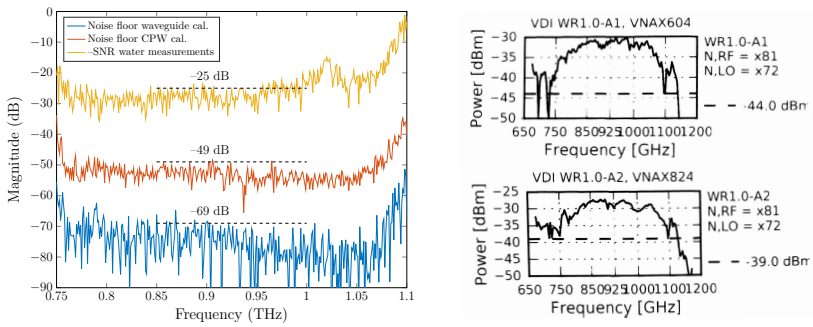

(a) **(b)**

Figure 4.8: Measurements exhibit a high dynamic range across the band. **(a)** Noise floor for the frequency extenders waveguide calibration and the CPW calibration. The frequency averaged dynamic range is 49 dB for PGL calibration and 69 dB for the frequency extender calibration. **(b)** Output power across the frequency band for the used frequency extenders, as shown in their specifications.

CHAPTER 5

Concluding remarks and future work

THz spectroscopy of aqueous samples allows analysing fundamental processes of biomolecules in their native environment. One of the main challenges of THz spectroscopy of aqueous samples, especially in on-chip configuration, is the high absorption of water of THz waves. This thesis has focused on developing a THz spectroscopy on-chip sensor for high-loss aqueous samples using VNA. The high dynamic range of the VNA allows measuring high-loss aqueous samples at THz frequencies, obtaining relatively high measurement SNR (an average of 25 dB when measuring water), key for detecting small signal changes. The proposed method is a first step towards a high-sensitivity and miniaturised system for THz spectroscopy system based on RF-technology.

To maximise the measurements' sensitivity, two different planar waveguides, CPW and PGL, were designed and fabricated in an ultra-thin (23 µm) low-permittivity substrate, minimising radiation losses. The thin substrate was supported by a mechanical substrate in order to isolate the planar waveguides from the metal chuck of the probe-station. The supporting substrate has shown a major impact in the radiation losses of the PGL, whereas for the CPW, with a more confined field, it didn't show a significant impact. Dedicated calibration standards were included in the chip, for both CPW and

PGL. In this work, PGL calibration standards were developed and verified for the first time. The CPW sensing structures were integrated with a microfluidic channel to characterise aqueous samples. The low loss of the sensing structures, combined with the high dynamic range of the VNA, allowed to characterise high-loss liquid samples like water from 750 GHz to 1100 GHz. Similar attempts to measure aqueous solutions with chips using time-domain spectroscopy, either lacked the SNR to analyse water samples over 0.5 THz or had to keep the sample away from the field in the planar transmission line used.

The presented method used ground-signal-ground THz probes for measuring the chips, but this approach introduces considerable losses. One way of maximising the dynamic range of the setup in the future would be the integration of the chip into a waveguide block directly attached to the frequency extenders.

Another aspect that could be improved in the future is the microfluidic channel. The microfluidic channel used in this work was mechanically clamped to the supporting substrate, introducing leakage problems. Fixing the microfluidic channel to the substrate would increase the repeatability of the measurements and accuracy.

Finally, the increase of repeatability in the reflection measurements would enable applying more complex two-tier calibration techniques to characterise the samples such as the line-line method described in the background of this thesis.

In the long term, to combine in the same chip the possibility of performing THz spectroscopy and sample alignment would have a major impact on the study of protein THz dynamics in solution. The alignment would enhance the proteins spectroscopic response, enabling THz spectroscopic signatures to be resolved in water.

CHAPTER 6

Summary of appended papers

Paper A

Multiline TRL Calibration Standards for S-parameter Measurement of Planar Goubau Lines from 0.75 THz to 1.1 THz

In this work, we developed a calibration standard for planar Goubau lines based on Through-Reflect-Line (TRL) standards. The calibration standards are validated with an established CPW calibration and with the proposed PGL calibration, showing good agreement with simulations in both cases. The calibration is used to demonstrate measurements of a 1 mm long PGL between 0.75 THz to 1.1 THz, with losses between 0.13 Np/mm to 0.35 Np/mm, negligible dispersion and wide-band characteristics. The proposed calibration standard opens up possibilities for studying and measuring the PGL and its circuit elements in detail.
My contribution: Design, fabrication, measurements, writing the article.

Paper B

Transmission Loss in Coplanar Waveguide and Planar Goubau Line between 0.75 THz and 1.1 THz

In this work, we compared the losses of 1 mm CPW and PGL, under two circumstances: with the polyethene supporting substrate below the device, and with the device being suspended on air. The CPW has a lower attenuation constant than the PGL if the supporting substrate is present below the devices. When the supporting substrate is removed from below the measured device, the attenuation constant of the CPW's remains unaltered, whereas the PGL's drops drastically, becoming more power-efficient than the CPW.
My contribution: Design, fabrication, measurements, writing the article.

Paper C

On-Chip Characterization of High-Loss Liquids between 750 GHz and 1100 GHz

In this work, we did THz transmission spectroscopy of high-loss aqueous samples using a chip excited with VNA and probes. The chip integrated CPWs and microfluidic channels, which would guide and control sample volumes. Aqueous samples are relevant in that they're the native environment for biological samples, and their extreme absorption poses a big challenge to chip measurements. Similar attempts using THz time-domain spectroscopy in chips, could not resolve water measurements above 0.5 THz or had to avoid having the sample on the transmission line's region with strongest field intensity, losing sensitivity. The proposed solution yielded high-SNR measurements and takes a step towards a miniaturised system for THz spectroscopy of high-loss liquids.
My contribution: Design of chip, fabrication, measurements, modelling, writing the article.

References

[1] T. Phillips and J. Keene, "Submillimeter astronomy (heterodyne spectroscopy)", *Proceedings of the IEEE*, vol. 80, no. 11, pp. 1662–1678, 1992. DOI: 10.1109/5.175248.

[2] H. J. Song and T. Nagatsuma, "Present and future of terahertz communications", *IEEE Transactions on Terahertz Science and Technology*, vol. 1, no. 1, pp. 256–263, 2011. DOI: 10.1109/TTHZ.2011.2159552.

[3] J. A. Zeitler, P. F. Taday, D. A. Newnham, M. Pepper, K. C. Gordon, and T. Rades, "Terahertz pulsed spectroscopy and imaging in the pharmaceutical setting - a review", *Journal of Pharmacy and Pharmacology*, vol. 59, no. 2, pp. 209–223, Feb. 2007. DOI: 10.1211/jpp.59.2.0008.

[4] M. R. Leahy-Hoppa, M. J. Fitch, X. Zheng, L. M. Hayden, and R. Osiander, "Wideband terahertz spectroscopy of explosives", *Chemical Physics Letters*, vol. 434, no. 4-6, pp. 227–230, 2007. DOI: 10.1016/j.cplett.2006.12.015.

[5] E. Pickwell and V. P. Wallace, "Biomedical applications of terahertz technology", *Journal of Physics D: Applied Physics*, vol. 39, no. 17, 2006. DOI: 10.1088/0022-3727/39/17/R01.

[6] A. Markelz, S. Whitmire, J. Hillebrecht, and R. Birge, "THz time domain spectroscopy of biomolecular conformational modes", *Physics in Medicine and Biology*, vol. 47, no. 21, pp. 3797–3805, 2002. DOI: 10.1088/0031-9155/47/21/318.

[7] N. Laman, S. S. Harsha, D. Grischkowsky, and J. S. Melinger, "High-resolution waveguide THz spectroscopy of biological molecules", *Biophysical Journal*, vol. 94, no. 3, pp. 1010–1020, 2008. DOI: 10.1529/biophysj.107.113647.

[8] X. Yang, X. Zhao, K. Yang, Y. Y. Liu, Y. Y. Liu, W. Fu, and Y. Luo, "Biomedical Applications of Terahertz Spectroscopy and Imaging", *Trends in Biotechnology*, vol. 34, no. 10, pp. 810–824, 2016. DOI: 10.1016/j.tibtech.2016.04.008.

[9] S. P. Mickan, A. Menikh, H. Liu, C. A. Mannella, R. Maccoll, D. Abbott, J. Munch, and X.-c. Zhang, "Label-free bioaffinity detection using terahertz", *Physics in medicine and biology*, vol. 47, pp. 3789–3795, 2002.

[10] M. Brucherseifer, M. Nagel, P. Haring Bolivar, H. Kurz, A. Bosserhoff, and R. Büttner, "Label-free probing of the binding state of DNA by time-domain terahertz sensing", *Applied Physics Letters*, vol. 77, no. 24, pp. 4049–4051, Dec. 2000. DOI: 10.1063/1.1332415.

[11] M. Nagel, P. Haring Bolivar, M. Brucherseifer, H. Kurz, A. Bosserhoff, and R. Büttner, "Integrated planar terahertz resonators for femtomolar sensitivity label-free detection of DNA hybridization", *Applied Optics*, vol. 41, no. 10, p. 2074, 2002. DOI: 10.1364/AO.41.002074.

[12] M. van Exter and D. R. Grischkowsky, "Characterization of an Optoelectronic Terahertz Beam System", *IEEE Transactions on Microwave Theory and Techniques*, vol. 38, no. 11, pp. 1684–1691, 1990. DOI: 10.1109/22.60016.

[13] M. Naftaly and R. Dudley, "Methodologies for determining the dynamic ranges and signal-to-noise ratios of terahertz time-domain spectrometers", *Optics Letters*, vol. 34, no. 8, p. 1213, Apr. 2009. DOI: 10.1364/ol.34.001213.

[14] J. T. Kindt and C. A. Schmuttenmaer, "Far-Infrared Dielectric Properties of Polar Liquids Probed by Femtosecond Terahertz Pulse Spectroscopy", *The Journal of Physical Chemistry*, 1996. DOI: 10.1021/jp960141g.

[15] L. Thrane, R. H. Jacobsen, P. U. Jepsen, and S. R. Keiding, "THz reflection spectroscopy of liquid water", *Chemical Physics Letters*, vol. 240, no. 4, pp. 330–333, 1995. DOI: 10.1016/0009-2614(95)00543-D.

[16] J. Kitagawa, T. Ohkubo, M. Onuma, and Y. Kadoya, "THz spectroscopic characterization of biomolecule/water systems by compact sensor chips", *Applied Physics Letters*, vol. 89, no. 4, p. 41 114, 2006. DOI: 10.1063/1.2236295.

[17] M. Swithenbank, A. D. Burnett, C. Russell, L. H. Li, A. G. Davies, E. H. Linfield, J. E. Cunningham, and C. D. Wood, "On-Chip Terahertz-Frequency Measurements of Liquids", *Analytical Chemistry*, vol. 89, no. 15, pp. 7981–7987, Aug. 2017. DOI: 10.1021/acs.analchem.7b01235.

[18] D. K. George, A. Charkhesht, and N. Q. Vinh, "New terahertz dielectric spectroscopy for the study of aqueous solutions", *Review of Scientific Instruments*, vol. 86, no. 12, p. 123 105, 2015. DOI: 10.1063/1.4936986.

[19] N. M. Ridler and R. G. Clarke, "Establishing Traceability to the International System of Units for Scattering Parameter Measurements from 750 GHz to 1.1 THz", *IEEE Transactions on Terahertz Science and Technology*, vol. 6, no. 1, pp. 2–11, 2016. DOI: 10.1109/TTHZ.2015.2502068.

[20] R. F. Bauer and P. Penfield, "De-Embedding and Unterminating", *IEEE Transactions on Microwave Theory and Techniques*, vol. 22, no. 3, pp. 282–288, 1974. DOI: 10.1109/TMTT.1974.1128212.

[21] M. F. Bauwens, N. Alijabbari, A. W. Lichtenberger, N. S. Barker, and R. M. Weikle, "A 1.1 THz micromachined on-wafer probe", in *2014 IEEE MTT-S International Microwave Symposium (IMS2014)*, Tampa, FL, 2014, pp. 1–4. DOI: 10.1109/MWSYM.2014.6848607.

[22] K. Grenier, D. Dubuc, P.-e. Poleni, and M. Kumemura, "Integrated Broadband Microwave and Microfluidic Sensor Dedicated to Bioengineering", vol. 57, no. 12, pp. 3246–3253, 2009. DOI: 10.1109/TMTT.2009.2034226.

[23] H. Rodilla, A. A. Kim, G. D. Jeffries, J. Vukusic, A. Jesorka, and J. Stake, "Millimeter-wave sensor based on a $\lambda/2$-line resonator for identification and dielectric characterization of non-ionic surfactants", *Scientific Reports*, vol. 6, no. October 2015, pp. 1–5, 2016. DOI: 10.1038/srep19523.

[24] S. Liu, I. Ocket, M. Cauwe, D. Schreurs, and B. Nauwelaers, "Sensitivity analysis of broadband on-wafer dielectric spectroscopy of yeast cell suspensions up to 110 GHz", *IEEE Microwave and Wireless Components Letters*, vol. 25, no. 3, pp. 199–201, 2015. DOI: 10.1109/LMWC.2015.2390542.

[25] K. A. Niessen, M. Xu, A. Paciaroni, A. Orecchini, E. H. Snell, and A. G. Markelz, "Moving in the Right Direction: Protein Vibrational Steering Function", *Biophysical Journal*, vol. 112, no. 5, pp. 933–942, 2017. DOI: 10.1016/j.bpj.2016.12.049.

[26] D. A. Bruggeman, "Berechnung verschiedener physikalischer Konstanten von heterogenen Substanzen. I. Dielektrizitätskonstanten und Leitfähigkeiten der Mischkörper aus isotropen Substanzen", *Annalen der Physik*, vol. 416, no. 7, pp. 636–664, 1935. DOI: 10.1002/andp.19354160705.

[27] H. Looyenga, "Dielectric constants of heterogeneous mixtures", *Physica*, vol. 31, no. 3, pp. 401–406, 1965. DOI: 10.1016/0031-8914(65)90045-5.

[28] S. M. Puranik, A. C. Kumbharkhane, and S. C. Mehrotra, "The static permittivity of binary mixtures using an improved bruggeman model", *Journal of Molecular Liquids*, vol. 59, no. 2-3, pp. 173–177, 1994. DOI: 10.1016/0167-7322(93)00665-6.

[29] P. L. Richards, "High-Resolution Fourier Transform Spectroscopy in the Far-Infrared", *Journal of the Optical Society of America*, vol. 54, no. 12, p. 1474, 1964. DOI: 10.1364/josa.54.001474.

[30] V. Skoromets, H. Němec, V. Goian, S. Kamba, and P. Kužel, "Performance Comparison of Time-Domain Terahertz, Multi-terahertz, and Fourier Transform Infrared Spectroscopies", *Journal of Infrared, Millimeter, and Terahertz Waves*, vol. 39, no. 12, pp. 1249–1263, 2018. DOI: 10.1007/s10762-018-0544-9.

[31] S. S. Dhillon, M. S. Vitiello, E. H. Linfield, A. G. Davies, M. C. Hoffmann, J. Booske, C. Paoloni, M. Gensch, P. Weightman, G. P. Williams, E. Castro-Camus, D. R. Cumming, F. Simoens, I. Escorcia-Carranza, J. Grant, S. Lucyszyn, M. Kuwata-Gonokami, K. Konishi, M. Koch, C. A. Schmuttenmaer, T. L. Cocker, R. Huber, A. G. Markelz, Z. D. Taylor, V. P. Wallace, J. Axel Zeitler, J. Sibik, T. M. Korter, B. Ellison, S.

Rea, P. Goldsmith, K. B. Cooper, R. Appleby, D. Pardo, P. G. Huggard, V. Krozer, H. Shams, M. Fice, C. Renaud, A. Seeds, A. Stöhr, M. Naftaly, N. Ridler, R. Clarke, J. E. Cunningham, and M. B. Johnston, "The 2017 terahertz science and technology roadmap", *Journal of Physics D: Applied Physics*, vol. 50, no. 4, 2017. DOI: 10.1088/1361-6463/50/4/043001.

[32] D. H. Auston and K. P. Cheung, "Coherent time-domain far-infrared spectroscopy", *Journal of the Optical Society of America B*, vol. 2, no. 4, p. 606, Apr. 1985. DOI: 10.1364/josab.2.000606.

[33] K. Minoshima, T. Yasui, K. Kawamoto, T. Araki, H. Inaba, Y. Sakaguchi, M. Jewariya, F. Hindle, and Y.-D. Hsieh, "Enhancement of spectral resolution and accuracy in asynchronous-optical-sampling terahertz time-domain spectroscopy for low-pressure gas-phase analysis", *Optics Express*, vol. 20, no. 14, pp. 15 071–15 078, 2012. DOI: 10.1364/oe.20.015071.

[34] D. Koller, S. Durant, C. Rowland, E. Bryerton, and J. Hesler, "Initial measurements with WM164 (1.1-1.5THz) VNA extenders", in *2016 41st International Conference on Infrared, Millimeter, and Terahertz Waves (IRMMW-THz)*, Copenhagen, 2016, pp. 1–2. DOI: 10.1109/IRMMW-THz.2016.7758434.

[35] T. W. Crowe, W. C. Peatman, P. A. Wood, and X. Liu, "GaAs Schottky barrier diodes for THz applications", *IEEE MTT-S International Microwave Symposium Digest*, vol. 2, no. 11, pp. 1141–1144, 1992. DOI: 10.1109/mwsym.1992.188196.

[36] N. M. Ridler and M. J. Salter, "Evaluating and expressing uncertainty in complex S-parameter measurements", in *56th ARFTG Conference Digest: Metrology and Test for RF Telecommunications, ARFTG 2000*, 2000. DOI: 10.1109/ARFTG.2000.327429.

[37] D. F. Williams, R. B. Marks, and A. Davidson, "Comparison of On-Wafer Calibrations", *ARFTG Conference Digest-Winter, 38th*, vol. 20, pp. 68–81, 1991. DOI: 10.1109/ARFTG.1991.324040.

[38] H. J. Eul and B. Schiek, "A Generalized Theory and New Calibration Procedures for Network Analyzer Self-Calibration", *IEEE Transactions on Microwave Theory and Techniques*, vol. 39, no. 4, pp. 724–731, 1991. DOI: 10.1109/22.76439.

[39] S. Rehnmark, "On the Calibration Process of Automatic Network Analyzer Systems", *IEEE Transactions on Microwave Theory and Techniques*, vol. 22, no. 4, pp. 457–458, 1974. DOI: 10.1109/TMTT.1974.1128250.

[40] R. B. Marks, "Formulations of the Basic Vector Network Analyzer Error Model including Switch-Terms", *50th ARFTG Conference Digest*, vol. 32, pp. 115–126, 1997. DOI: 10.1109/ARFTG.1997.327265.

[41] ——, "A Multiline Method of Network Analyzer Calibration", *IEEE Transactions on Microwave Theory and Techniques*, vol. 39, no. 7, pp. 1205–1215, 1991. DOI: 10.1109/22.85388.

[42] D. F. Williams, F. J. Schmückle, R. Doerner, G. N. Phung, U. Arz, and W. Heinrich, "Crosstalk corrections for coplanar-waveguide scattering-parameter calibrations", *IEEE Transactions on Microwave Theory and Techniques*, vol. 62, no. 8, pp. 1748–1761, 2014. DOI: 10.1109/TMTT.2014.2331623.

[43] G. N. Phung, F. J. Schmuckle, R. Doerner, B. Kahne, T. Fritzsch, U. Arz, and W. Heinrich, "Influence of microwave probes on calibrated on-wafer measurements", *IEEE Transactions on Microwave Theory and Techniques*, vol. 67, no. 5, pp. 1892–1900, 2019. DOI: 10.1109/TMTT.2019.2903400.

[44] R. E. Collin, "Waves on a Lossy Transmission Line", in *Foundations for Microwave Engineering*, 2nd, Hoboken, New Jersey: Wiley InterScience, 2001, ch. 3, pp. 86–89. DOI: 10.1109/9780470544662.ch3.

[45] A. Sommerfeld, "Ueber die Fortpflanzung elektrodynamischer Wellen längs eines Drahtes", *Annalen der Physik*, vol. 303, no. 2, pp. 233–290, 1899. DOI: 10.1002/andp.18993030202.

[46] F. Harms, "Elektromagnetische Wellen an einem Draht mit isolierender zylindrischer Hülle", *Annalen der Physik*, vol. 328, no. 6, pp. 44–60, 1907. DOI: 10.1002/andp.19073280603.

[47] G. Goubau, "Surface waves and their application to transmission lines", *Journal of Applied Physics*, vol. 21, no. 11, pp. 1119–1128, 1950. DOI: 10.1063/1.1699553.

[48] ——, "Single-Conductor Surface-Wave Transmission Lines", *Proceedings of the IRE*, vol. 39, no. 6, pp. 619–624, 1951. DOI: 10.1109/JRPROC.1951.233782.

[49] H. Barlow and A. Cullen, "Surface waves", *Proceedings of the IEE - Part III: Radio and Communication Engineering*, vol. 100, no. 68, pp. 329–341, 1953. DOI: 10.1049/pi-3.1953.0068.

[50] K. Wang and D. M. Mittleman, "Metal wires for terahertz wave guiding", *Nature*, vol. 432, no. November, pp. 376–379, Nov. 2004. DOI: 10.1038/nature03040.

[51] N. C. J. Van Der Valk and P. C. M. Planken, "Effect of a dielectric coating on terahertz surface plasmon polaritons on metal wires", *Applied Physics Letters*, vol. 87, no. 7, p. 071 106, Aug. 2005. DOI: 10.1063/1.2011773.

[52] Y. Xu and R. G. R. G. Bosisio, "A study of planar Goubau lines (PGLs) for millimeter- and submillimeter-wave integrated circuits (ICs)", *Microwave and Optical Technology Letters*, vol. 43, no. 4, pp. 290–293, Nov. 2004. DOI: 10.1002/mop.20448.

[53] A. Treizebré, T. Akalin, and B. Bocquet, "Planar excitation of goubau transmission lines for THz BioMEMS", *IEEE Microwave and Wireless Components Letters*, vol. 15, no. 12, pp. 886–888, 2005. DOI: 10.1109/LMWC.2005.859976.

[54] C. P. Wen, "Coplanar Waveguide: A Surface Strip Transmission Line Suitable for Nonreciprocal Gyromagnetic Device Applications", *IEEE Transactions on Microwave Theory and Techniques*, vol. 17, no. 12, pp. 1087–1090, 1969. DOI: 10.1109/TMTT.1969.1127105.

[55] D. Debuisson, A. Treizebré, T. Houssin, E. Leclerc, D. Bartès-Biesel, D. Legrand, J. Mazurier, S. Arscott, B. Bocquet, and V. Senez, "Nanoscale devices for online dielectric spectroscopy of biological cells", *Physiological Measurement*, vol. 29, no. 6, 2008. DOI: 10.1088/0967-3334/29/6/S19.

[56] D. B. Rutledge, D. P. Neikirk, and D. P. Kasilingam, "Integrated-Circuit Antennas", in *Infrared and millimeter waves*, vol. 10, New York: Academic, 1983, ch. 1, pp. 28–34.

[57] M. Riaziat, R. Majidi-Ahy, and I. J. Feng, "Propagation Modes and Dispersion Characteristics of Coplanar Waveguides", *IEEE Transactions on Microwave Theory and Techniques*, vol. 38, no. 3, pp. 245–251, 1990. DOI: 10.1109/22.45333.

[58] S. S. Attwood, *Surface-wave propagation over a coated plane conductor*, 1951. DOI: 10.1063/1.1699991.

[59] R. E. Collin, "Surface Waveguides", in *Field Theory of Guided Waves*, vol. 30, Wiley-IEEE Press, 1991, ch. 11, pp. 697–748. DOI: 10.1109/9780470544648.ch11.

[60] D. B. Rutledge, S. E. Schwarz, and A. T. Adams, "Infrared and submillimetre antennas", *Infrared Physics*, vol. 18, no. 5-6, pp. 713–729, 1978. DOI: 10.1016/0020-0891(78)90094-5.

[61] A. A. Oliner and H. Shigesawa, "New Interesting Leakage Behavior on Coplanar Waveguides of Finite and Infinite Widths", *IEEE Transactions on Microwave Theory and Techniques*, vol. 39, no. 12, pp. 2130–2137, 1991. DOI: 10.1109/22.106555.

[62] X. Bao, S. Liu, I. Ocket, J. Bao, D. Kil, M. Zhang, B. Puers, D. Schreurs, and B. Nauwelaers, "A Multiline Multimaterial Calibration Method for Liquid Characterization", *IEEE Microwave and Wireless Components Letters*, vol. 28, no. 8, pp. 732–734, Aug. 2018. DOI: 10.1109/LMWC.2018.2845704.

[63] D. A. Frickey, "Conversions Between S, Z, Y, h, ABCD, and T Parameters which are Valid for Complex Source and Load Impedances", *IEEE Transactions on Microwave Theory and Techniques*, vol. 42, no. 2, pp. 205–211, 1994. DOI: 10.1109/22.275248.

[64] N. Fuse, T. Takahashi, Y. Ohki, R. Sato, M. Mizuno, and K. Fukunaga, "Terahertz Spectroscopy as a New Tool for Insulating Material Analysis and Condition Monitoring", *IEEE Insulating Magazine*, vol. 27, no. 3, pp. 26–35, 2011. DOI: 10.1109/MEI.2011.5871366.

[65] E. Chen and S. Y. Chou, "Characteristics of coplanar transmission lines on multilayer substrates: modeling and experiments", *IEEE Transactions on Microwave Theory and Techniques*, vol. 45, no. 6, pp. 939–945, 1997. DOI: 10.1109/22.588606.

[66] X. Bao, S. Liu, I. Ocket, J. Bao, D. Schreurs, S. Zhang, C. Cheng, K. Feng, and B. Nauwelaers, "A General Line-Line Method for Dielectric Material Characterization Using Conductors with the Same Cross-Sectional Geometry", *IEEE Microwave and Wireless Components Letters*, vol. 28, no. 4, pp. 356–358, Apr. 2018. DOI: 10.1109/LMWC.2018.2809041.

[67] Y. Yomogida, Y. Sato, R. Nozaki, T. Mishina, and J. Nakahara, "Comparative study of boson peak in normal and secondary alcohols with terahertz time-domain spectroscopy", *Physica B: Condensed Matter*, vol. 405, no. 9, pp. 2208–2212, 2010. DOI: 10.1016/j.physb.2010.02.010.

[68] Y. Yomogida, Y. Sato, R. Nozaki, T. Mishina, and J. Nakahara, "Comparative dielectric study of monohydric alcohols with terahertz time-domain spectroscopy", *Journal of Molecular Structure*, vol. 981, no. 1-3, pp. 173–178, 2010. DOI: 10.1016/j.molstruc.2010.08.002.

[69] M. Swithenbank, C. Russell, A. D. Burnett, L. H. Li, A. G. Davies, E. H. Linfield, J. E. Cunningham, and C. D. Wood, "Accurate parameter extraction from liquids measured using on-chip terahertz spectroscopy", in *International Conference on Infrared, Millimeter, and Terahertz Waves, IRMMW-THz*, Copenhagen, 2016, pp. 1–2. DOI: 10.1109/IRMMW-THz.2016.7758409.

[70] P. U. Jepsen, U. Møller, and H. Merbold, "Investigation of aqueous alcohol and sugar solutions with reflection terahertz time-domain spectroscopy", *Optics Express*, vol. 15, no. 22, p. 14 717, 2007. DOI: 10.1364/OE.15.014717.

[71] D. J. Segelstein, "The complex refractive index of water", PhD thesis, Department of Physics, University of Missouri–Kansas City, 1981, p. 167.

[72] N. Q. Vinh, M. S. Sherwin, S. J. Allen, D. K. George, A. J. Rahmani, and K. W. Plaxco, "High-precision gigahertz-to-terahertz spectroscopy of aqueous salt solutions as a probe of the femtosecond-to-picosecond dynamics of liquid water", *Journal of Chemical Physics*, vol. 142, no. 16, p. 164 502, 2015. DOI: 10.1063/1.4918708.

[73] J. N. Lee, C. Park, and G. M. Whitesides, "Solvent Compatibility of Poly(dimethylsiloxane)-Based Microfluidic Devices", *Analytical Chemistry*, vol. 75, no. 23, pp. 6544–6554, 2003. DOI: 10.1021/ac0346712.

APPENDED PAPERS

Paper A

Multiline TRL Calibration Standards for S-parameter Measurement of Planar Goubau Lines from 0.75 THz to 1.1 THz

J. Cabello-Sánchez, H. Rodilla, V. Drakinskiy and J. Stake

2018 IEEE/MTT-S International Microwave Symposium - IMS
Philadelphia, PA, 2018, pp. 879-882,
 DOI: 10.1109/MWSYM.2018.8439138

Multiline TRL Calibration Standards for S-parameter Measurement of Planar Goubau Lines from 0.75 THz to 1.1 THz

Juan Cabello-Sánchez, Helena Rodilla, Vladimir Drakinskiy and Jan Stake
Chalmers University of Technology, 412 96 Gothenburg, Sweden

***Abstract*—We present a multiline Thru-Reflect-Line (TRL) calibration standard for Planar Goubau Line (PGL) which allows setting the calibration plane along the PGL and thus removing the effect of the embedding structure. This opens the possibility of characterizing PGL-circuits. The presented structures were used for calibrating S-parameters measurements between 0.75 THz and 1.1 THz to characterize a 1 mm long and 10 µm wide PGL. The line shows negligible dispersion with an effective relative permittivity of 2.0 and an attenuation constant lower than 0.35 Np/mm (0.65 dB/λ).**

***Index Terms*— Calibration, Multiline TRL, On-wafer THz measurements, Planar Goubau Lines, S-parameter characterization, Terahertz circuits.**

I. Introduction

The Planar Goubau Line (PGL) [1]-[4] is a groundless single conductor waveguide consisting of a metal strip supported by a dielectric substrate (see Fig. 1 a). This waveguide is the two-dimensional counterpart of Goubau's dielectric coated single wire waveguide [5]-[6], which in turn is based on the finite-conductivity wire waveguide studied by Sommerfeld [7] in 1899. In both the Goubau and the Sommerfeld lines, the field propagates as a surface wave [8]-[9].

As the Sommerfeld and Goubau line, the PGL's propagating mode is transverse magnetic and has a quasi-radial electric field around the conductor. Due to its single-conductor nature, the field in the PGL has a large extension compared to other multi-conductor transmission lines used at terahertz (THz) frequencies, such as Coplanar Waveguide (CPW), while it exhibits negligible dispersion across a wide bandwidth. This makes the PGL a suitable candidate for sensing applications [2], where interaction with a larger volume is required. Additionally, its physical geometry favors liquid sample deposition around the line.

To excite the PGL using ground-signal-ground probes, a CPW to PGL transition [3] is needed (Fig. 1 b)). Therefore, unless the calibration plane is set after the CPW-PGL transition, the measurements will include the impact of the transition, which might be undesirable. To the best of the authors' knowledge, no reported calibration structures exist which allow to de-embed these transitions.

In this paper, we present multiline Thru-Reflect-Line (TRL) calibration standards which allow setting the calibration plane at the PGL, and thus opening the possibility to accurately characterize PGL based circuits [4]. Using the aforementioned TRL calibration structures, a 10 µm wide and 1 mm long PGL on a 23 µm thin polyethylene terephthalate (PET) film was characterized from 0.75 THz to 1.1 THz.

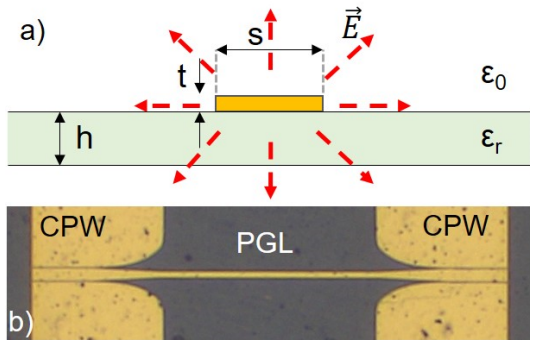

Fig. 1 a) Sketch of the cross-section of the PGL where the electric field is represented by dashed arrows. b) Microscope picture of a PGL showing the CPW-PGL transition needed to contact with ground-signal-ground probes.

II. Method

A. PGL Design

To efficiently excite a PGL with ground-signal-ground probes, one first needs to excite a CPW due to its suitable probing geometry. This CPW can then change its dimensions to progressively couple its even mode into a PGL's propagating mode. This can be done by separating the CPW's ground planes while changing the width of the CPW's central conductor (Fig. 1 b)) [3]. However, this change in the CPW's gap and conductor width dimensions will produce a change in impedance, which will cause reflections. In the transition used, the conductor and gap dimensions were designed to vary its impedance value using a geometric progression to minimize reflections, while simultaneously avoiding using small CPW strip and gap widths, which increase line losses.

To maximize the power delivered to the PGL, the length of the transition was optimized resulting in a trade-off between reflections and line losses. Additionally, if the transition length is a multiple of one half-wavelength it will produce minimum reflections, thus the length was chosen as the multiple of half-wavelength (at the center of the band) which maximized the power delivered to the PGL.

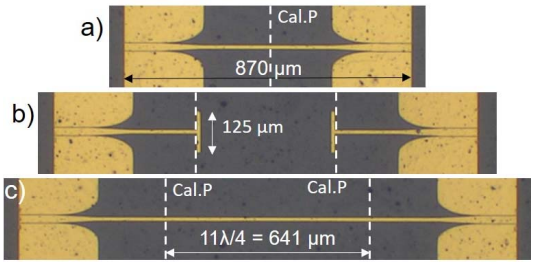

Fig. 2 Microscope image of the fabricated calibration standard, showing: a) thru, b) reflect and c) 11λ/4 line. Dashed lines indicate the calibration plane. Figures are shown to scale.

To design the transition, electromagnetic simulations of the structure were performed using commercial finite integration technique software.

To decrease substrate modes, which cause dispersion and radiation losses, it is recommended to use thin and low permittivity substrates, since they increase the substrate mode's cutoff frequency [10]. Thus a 23 µm thin PET film ($\varepsilon_r = 3.15$ and $\tan(\delta) = 0.017$ at 1 THz [11]) was selected as the supporting substrate.

B. Multiline TRL Calibration Standard Design

The TRL calibration method [12] is a widely used approach at THz frequencies [13]-[14] since it requires no loads, which are challenging to fabricate with precision at THz frequencies. To minimize the effects of random errors, and improve the accuracy and bandwidth of the TRL calibration, multiple lines with different electrical lengths can be included in the calibration substrate [15].

In the case of the PGL, the design of the thru and line standards is straightforward after the CPW-PGL transition has been designed (see Fig. 2 a) and c)). The thru standard had a probe-to-probe distance of 870 µm and the calibration lines had an additional PGL length of 58 µm (λ/4), 175 µm (3λ/4) and 641 µm (11λ/4) at 910 GHz (considering an effective dielectric permittivity of $\varepsilon_{eff} = 2$, obtained from simulations).

However, the design of a PGL-reflect is not as straightforward as it consists of a single conductor. The reflect was designed as a T-shaped structure by adding a λ/2 long perpendicular conducting strip (10 µm × 125 µm) at the end of an open PGL, as shown in Fig. 2 b). It should be noted that, despite resembling a dipole antenna, this structure has a single conductor and a wideband reflective behavior, thus not acting as an antenna.

The PGL and the calibration substrates were fabricated on the same substrate using e-beam lithography. A 350-nm thick layer of gold was evaporated on top of the 23-µm thick PET substrate, forming the conductor layer.

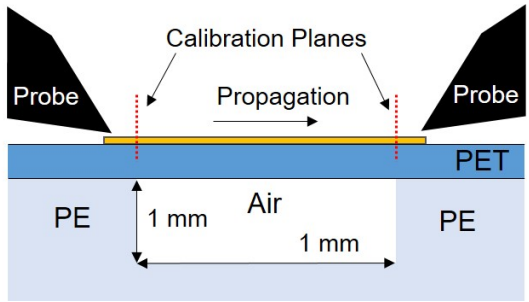

Fig. 3 Cross section sketch of the measurement procedure with the 1 mm long PGL deposited on the thin film of PET and suspended in the PE substrate holder. The PGL calibration planes are marked as discontinued red lines. Figure is not to scale.

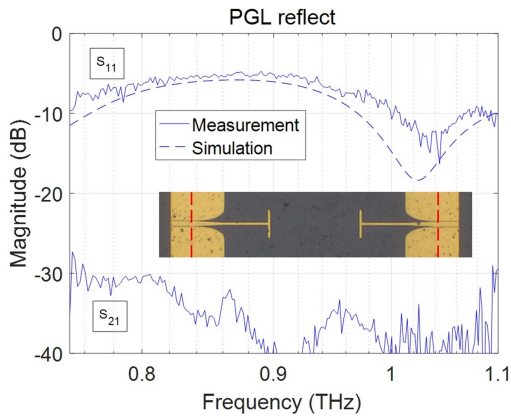

Fig. 4 S-parameter simulation (dashed line) and measurement (solid lines) from 0.75 THz to 1.1 THz of CPW-PGL transition followed by reflect element. Simulated S_{21} was bellow -95 dB in all the band. A CPW multiline TRL standard was used to calibrate the measurements. Inset shows the layout of the simulated and measured structure. Dashed line in inset indicates the location of the calibration plane, 105 µm into the 50 Ω CPW line of the CPW-PGL transition.

C. Measurement Set-up

The 2-port S-parameter measurements from 0.75 THz to 1.1 THz were performed using an Agilent N5242A PNA-X Network Analyzer connected to two VDI WR1.0SAX frequency extenders. The IF bandwidth of the VNA was set to 50 Hz. To probe the structures, ground-signal-ground Cascade T-Wave probes were used [16]. To minimize the phase noise to achieve a higher dynamic range in the measurements, external RF and LO sources were used (Keysight E8257D).

The fabricated wafer was placed on a polyethylene (PE) holder ($\varepsilon_r = 2.3$ and $\tan(\delta) = 0.004$ at 1 THz [11]). This PE holder separates the structures from the metal chuck of the

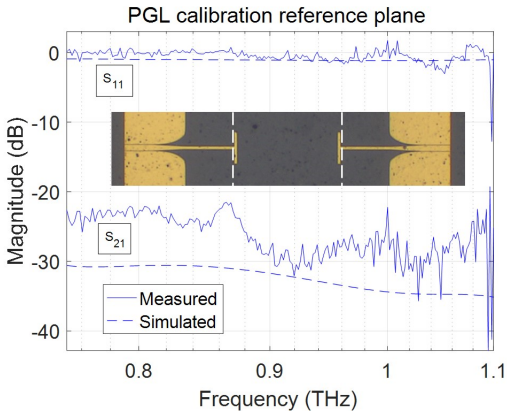

Fig. 5 S-parameter simulation (dashed lines) vs. measurement (solid lines) of reflect element using the proposed PGL multiline TRL standard. Simulation results give S_{11} values higher than -1.1 dB in all the band. Inset shows the layout of the simulated and measured structure. Dashed line in inset indicates the location of the PGL calibration reference plane.

probe station avoiding field coupling and ensuring the PGL mode propagation.

To avoid substrate modes in the PE holder and minimize the losses while keeping the mechanical support, 1 mm deep and 1 mm wide holes were micromachined in the PE holder (Fig. 3). With this configuration, the 1 mm long PGL has air as dielectric under the PET while maintaining the mechanical support under the probing area.

Two different calibration standards were included in the wafer for comparing measurements: the proposed PGL multiline TRL, that sets the calibration plane along the PGL, and a customized CPW multiline TRL standard, with a calibration plane set 105 µm into the 50 Ω CPW line (with a 23.5 µm wide conductor strip and 1.5 µm wide gap) of the CPW-PGL transition.

III. Results

First, to verify the behavior of the reflect of the proposed PGL TRL calibration substrate, the reflect structure was measured using the CPW multiline TRL standard. Measurements were compared with simulation results showing good agreement between the S_{11} and S_{21} (Fig. 4). The same S-parameter reflect simulation and measurements were repeated using the proposed PGL multiline TRL standard. Therein both simulated and measured S_{11} yielded high reflection results in all the band, having simulated S_{11} results higher than -1.1 dB in all the band (Fig. 5). Simulation and measurement results of S_{21} showed to have a desirable isolation and good agreement between them. Overall, the reflect standard is functional and behaves as expected.

Using the proposed PGL multi-line TRL standards, which allows the de-embedding of the CPW-PGL transition, a 1 mm

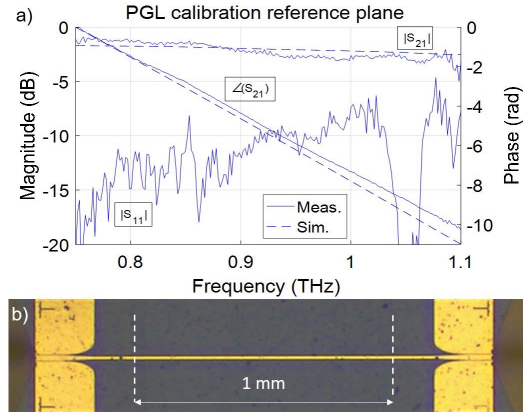

Fig. 6 a) S-parameter simulation (dashed lines) and measurements (solid lines) between 0.75 THz and 1.1 THz of a 10 µm wide and 1 mm long PGL using the proposed PGL multiline TRL calibration standard to calibrate the measurements. Simulated |S11| results lied bellow -30 dB in all the band. b) Microscope image of the 1 mm long PGL. Dashed lines indicate PGL calibration reference plane. The probes can be seen making contact at the edge of the CPWs.

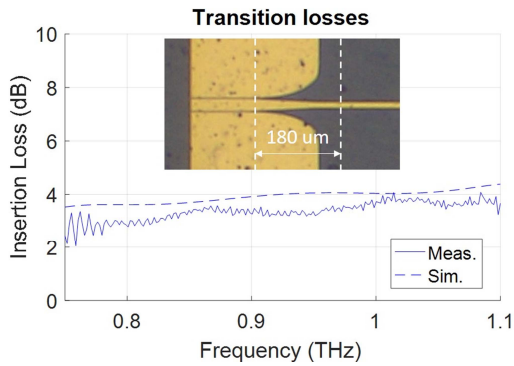

Fig. 7 Simulated (dashed line) and measured (solid line) insertion loss of the 180 µm long CPW-PGL transition. Inset shows the considered transition where dashed lines indicate its span.

long and 10 µm wide PGL on a 23 µm thick PET film suspended on air was measured. The S-parameter measurement results show S_{21} between -1.1 dB and -3.0 dB (Fig. 6) from 0.75 THz to 1.1 THz, which corresponds to an attenuation constant between 0.13 Np/mm and 0.35 Np/mm. Additionally, the phase and group velocity of the PGL showed to be approximately 71% of the speed of light ($\varepsilon_{eff} = 2.0$), with negligible dispersion across the band. Reflection (S_{11}) measurements exhibit a higher uncertainty than the transmission (S_{21}) due to its high dependence on probing conditions.

The proposed PGL multi-line TRL standards allowed to experimentally estimate the insertion loss of the designed CPW-

PGL transition, which has a length of 180 µm (Fig. 7). Insertion loss resulted in values between 2 dB and 4 dB in the entire band, which are considered to be low taking into account the operating frequency.

IV. Conclusion

A set of multiline TRL calibration standards has been designed, fabricated and used to characterize a PGL from 0.75 THz to 1.1 THz. Measurement results of the reflect element have shown to have a wideband high-reflective behavior, which allows the multiline TRL standard to de-embed all elements behind the PGL calibration reference plane. This opens the possibility of studying in detail this waveguide, circuit elements included in it and to enhance the PGL's sensing capabilities.

The measured 10 µm wide and 1 mm long PGL has shown to have low line losses (between 0.13 Np/mm and 0.35 Np/mm in the range 0.75 - 1.1 THz), negligible dispersion, and wide-band characteristics.

Acknowledgment

The authors would like to thank Johanna Hanning and Dr. Stella Bevilacqua for their support regarding THz metrology and measurements. This research was funded by the Swedish Research Council (*Vetenskapsrådet*).

References

[1] Xu and R. G. Bosisio, "A study of planar Goubau lines (PGLs) for millimeter-and submillimeter-wave integrated circuits (ICs)," *Microwave and optical technology letters*, vol. 43, no. 4, pp. 290–293, 2004.

[2] A. Treizebré, T. Akalin, and B. Bocquet, "Planar excitation of Goubau transmission lines for THz bioMEMS," *IEEE microwave and wireless components letters*, vol. 15, no. 12, pp. 886–888, 2005.

[3] A. Treizebré, B. Bocquet, Y. Xu, and R. G. Bosisio, "New THz excitation of planar Goubau line," *Microwave and Optical Technology Letters*, vol. 50, no. 11, pp. 2998–3001, 2008.

[4] Y. Xu, C. Nerguizian, and R. Bosisio, "Wideband planar Goubau line integrated circuit components at millimetre waves," *IET microwaves, antennas & propagation*, vol. 5, no. 8, pp. 882–885, 2011.

[5] G. Goubau, "Surface waves and their application to transmission lines," *Journal of Applied Physics*, vol. 21, no. 11, pp. 1119–1128, 1950.

[6] G. Goubau, "Single-conductor surface-wave transmission lines," *Proceedings of the IRE*, vol. 39, no. 6, pp. 619–624, 1951.

[7] A. Sommerfeld, "Ueber die fortpflanzung elektrodynamischer wellen längs eines drahtes," *Annalen der Physik*, vol. 303, no. 2, pp. 233–290,1899.

[8] H. Barlow and A. Cullen, "Surface waves," *Proceedings of the IEEE-Part III: Radio and Communication Engineering*, vol. 100, no. 68, pp. 329–341, 1953

[9] S. J. Orfanidis, Electromagnetic waves and antennas. Rutgers University New Brunswick, NJ, 2002.

[10] M. Riaziat, R. Majidi-Ahy, and I.-J. Feng, "Propagation modes and dispersion characteristics of coplanar waveguides," *IEEE transactions on microwave theory and techniques*, vol. 38, no. 3, pp. 245–251, 1990.

[11] N. Fuse, T. Takahashi, Y. Ohki, R. Sato, M. Mizuno, and K. Fukunaga, "Terahertz spectroscopy as a new tool for insulating material analysis and condition monitoring," *IEEE Electrical Insulation Magazine*, vol. 27, no. 3, 2011.

[12] G. F. Engen and C. A. Hoer, "Thru-reflect-line: An improved technique for calibrating the dual six-port automatic network analyzer," *IEEE transactions on microwave theory and techniques*, vol. 27, no. 12, pp. 987–993, 1979.

[13] Z. Popovic and E. N. Grossman, "THz metrology and instrumentation," *IEEE Transactions on Terahertz Science and Technology*, vol. 1, no. 1,pp. 133–144, 2011.

[14] J. Hanning, J. Stenarson, K. Yhland, P. J. Sobis, T. Bryllert, and J. Stake, "Single-flange 2-port TRL calibration for accurate THz S-parameter-measurements of waveguide integrated circuits," *IEEE Transactions on Terahertz Science and Technology*, vol. 4, no. 5, pp. 582–587, 2014.

[15] R. B. Marks, "A multiline method of network analyzer calibration," *IEEE Transactions on Microwave Theory and Techniques*, vol. 39, no. 7, pp. 1205–1215, 1991.

[16] M. F. Bauwens, N. Alijabbari, A. W. Lichtenberger, N. S. Barker, and R. M. Weikle, "A 1.1 THz micromachined on-wafer probe," In *Microwave Symposium (IMS), 2014 IEEE MTT-S International*.IEEE, 2014, pp.1–4.

Paper B

Transmission Loss in Coplanar Waveguide and Planar Goubau Line between 0.75 THz and 1.1 THz

J. Cabello-Sánchez, H. Rodilla, V. Drakinskiy and J. Stake

2018 43rd International Conference on Infrared, Millimeter, and Terahertz Waves (IRMMW-THz)
Nagoya, 2018, pp. 1-2,
 DOI: 10.1109/IRMMW-THz.2018.8510326

Transmission Loss in Coplanar Waveguide and Planar Goubau Line between 0.75 THz and 1.1 THz

J. Cabello-Sánchez, H. Rodilla, V. Drakinskiy and J. Stake
Chalmers University of Technology, 412 96 Gothenburg, Sweden

***Abstract*—In many cases, metallic planar waveguides are required in the design of integrated circuits. However, at terahertz frequencies, metallic planar waveguides present high losses, which make necessary the use more efficient waveguides to avoid power limitations. In this work, the attenuation constant of two popular planar waveguides for terahertz frequencies, Coplanar Waveguide (CPW) and Planar Goubau Line (PGL), are compared between 0.75 THz and 1.1 THz. To measure the PGL, its transition is deembeded using a multiline Thru-Reflect-Line calibration standard. Measurement results show a lower attenuation constant across the band for a PGL ($0.13\ mm^{-1} < \alpha < 0.39\ mm^{-1}$) than for a CPW ($0.68\ mm^{-1} < \alpha < 0.99\ mm^{-1}$) when an ultra-thin substrate is used suspended in air, which greatly reduces the substrate mode coupling from the PGL. These results put the PGL as a less lossy metallic planar waveguide for terahertz applications.**

I. INTRODUCTION

WAVEGUIDES are a fundamental part of most high-frequency electronic circuits. A lack of low-loss waveguides would pose severe constraints on most circuit designs. At terahertz (THz) frequencies, high losses in metallic waveguides together with a low available power severely reduces the signal to noise ratio, thus making loss minimization crucial for waveguides at this frequency band [1], [2]. High losses are accentuated when metallic planar waveguides are needed for chip integration, due to their higher losses compared to their non-planar counterparts. This creates the need to study and optimize the performance of metallic planar waveguides used at THz frequencies to expand the possibilities of THz chip design. In this context, we present a comparison of the attenuation constant of two popular metallic planar waveguides suitable for THz applications, Coplanar Waveguide (CPW) (Fig. 1.a) [3] and Planar Goubau Line (PGL) (Fig. 1.b) [4], [5], in addition to general guidelines on how can losses be minimized in these waveguides at THz frequencies.

II. METHOD

In this work, the attenuation of a 1 mm long CPW (Fig. 2.a) and a 1 mm long PGL (Fig. 2.b) are compared using on-wafer S-parameter measurements from 0.75 THz to 1.1 THz. The CPW, designed to suit the ground-signal-ground probes' dimensions [6], has a 23.5 µm wide strip, a 1.5 µm ground separation and a characteristic impedance of 50 Ω; while the PGL has a 10 µm wide conducting strip and an approximate characteristic impedance of 230 Ω. The PGL was excited with the probes using a CPW to PGL transition [7].

To minimize substrate mode excitation [8], [9], and thus reduce losses, we chose a 23 µm thick polyethylene terephthalate (PET) film (with a relative permittivity of $\varepsilon_r = 3.15$ and a loss tangent of $\tan(\delta) = 0.017$ at 1 THz [10]) as the substrate. The PET substrate was placed on top of a polyethylene (PE) holder ($\varepsilon_r = 2.3$ and $\tan(\delta) = 0.004$ at 1 THz [10]) during measurements to avoid coupling of the structures with the metal chuck from the measurement's set-up. The conducting strips of both the PGL and the CPW were fabricated using e-beam lithography and e-gun evaporation of 10 nm Ti and 350 nm Au.

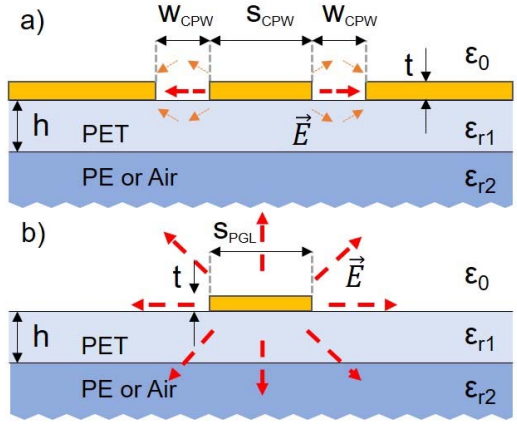

Fig. 1. Cross-section sketch of **a)** coplanar waveguide and **b)** planar Goubau line. Dashed lines indicate the electrical field of the main propagation mode in each waveguide. Both waveguides were measured in two environments: with PE ($\varepsilon_{r2} = 2.3$) or with air ($\varepsilon_{r2} = 1$) under the PET substrate.

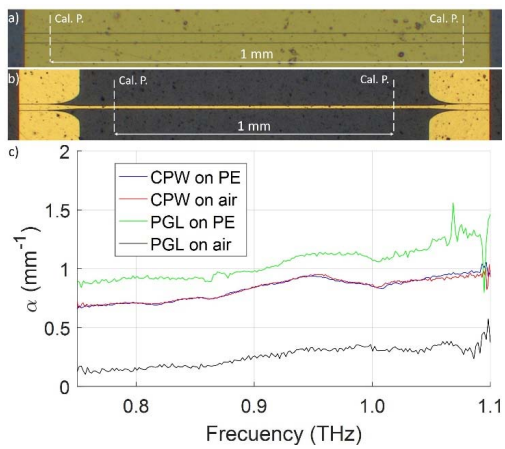

Fig. 2. a) Optical micrograph of the 1 mm long CPW with a 23.5 µm wide strip and ground separation of 1.5 µm. Vertical dashed lines indicate the location of the calibration planes. **b)** Optical micrograph of the 1 mm long and 10 µm wide PGL. Vertical dashed lines indicate the location of the calibration planes. Behind each calibration plane lies the CPW to PGL transition. **c)** Measured attenuation constant of the above structures having PE or air under the PET substrate.

The S-parameter measurements from 0.75 THz to 1.1 THz were performed using an Agilent N5242A PNA-X Network Analyzer attaching two VDI WR1.0SAX frequency extenders. To contact the planar structures, Cascade T-Wave ground-signal-ground probes [6] were used. The measurements were calibrated using multi-line TRL calibration standards [11], included in the PET substrate. To compare the PGL to the CPW without the effect of the PGL's transition, a dedicated calibration standard was used for each waveguide, CPW and PGL [12], which allowed setting the calibration plane along each line (see Fig 2.a and Fig 2.b). The waveguides were measured in two different environments: with PE under the PET substrate ($\varepsilon_{r1} = 3.15$; $\varepsilon_{r2} = 2.3$), or with air under the PET substrate ($\varepsilon_{r1} = 3.15$; $\varepsilon_{r2} = 1$), by micromachining a hole in the PE holder.

III. Results

When there is PE under the PET substrate ($\varepsilon_{r1} = 3.15$; $\varepsilon_{r2} = 2.3$), S-parameter measurement results of the 1 mm long CPW (Fig. 2.c) show an attenuation constant, α, between 0.68 mm^{-1} and 0.99 mm^{-1} and return loss above 15 dB across the band. On the other hand, measurements results of a 1 mm long PGL (Fig. 2 c) show 0.87 $mm^{-1} < \alpha < 1.38$ mm^{-1} and return loss above 15 dB across the band. Under these circumstances, there is an approximately 0.25 mm^{-1} lower attenuation constant across the band for the CPW than for the PGL.

When the PE under the PET substrate is removed ($\varepsilon_{r1} = 3.15$; $\varepsilon_{r2} = 1$), the CPW's S-parameter measurement results (Fig. 2.c) show negligible change. However, for the PGL there is an approximately 0.78 mm^{-1} decrease in the attenuation constant (0.13 $mm^{-1} < \alpha < 0.39$ mm^{-1}), compared to when there is PE under the PET substrate. In this case the PGL, with 0.39 $mm^{-1} < \alpha < 0.13$ mm^{-1} across the band, has an approximately 0.55 mm^{-1} lower attenuation constant than the CPW. These results suggest that the highly confined field in the CPW does not excite substrate modes in the PE under the PET substrate and that the attenuation is mainly caused by conductor and dielectric losses. In contrast, the PGL excites substrate modes in the presence of the PE holder, due to its lower field confinement, but has a fewer sum of conductor and dielectric losses compared to the CPW. Thus, to decrease losses in the PGL it's crucial to avoid substrate mode coupling.

For lowering the conductor losses in the CPW, it is necessary to increase the strip width and the strip-to-ground separation [13]. This comes at the cost of a higher tendency to excite substrate modes due to a lower confinement of the field. In the limit when conductor losses are minimized in the CPW, the ground planes would be too distant from the CPW's central strip to have an impact in the field, thus having a propagating mode similar to the PGL's.

Acknowledgment

This research was funded by the Swedish Research Council (*Vetenskapsrådet*).

References

[1] K. Wang and D. M. Mittleman, "Metal wires for terahertz wave guiding," *Nature*, vol. 432, no. November, pp. 376–379, Nov. 2004.

[2] F. Fesharaki, T. Djerafi, M. Chaker, and K. Wu, "Low-Loss and Low-Dispersion Transmission Line over DC-to-THz Spectrum," *IEEE Trans. Terahertz Sci. Technol.*, vol. 6, no. 4, pp. 611–618, 2016.

[3] C. P. Wen, "Coplanar Waveguide: A Surface Strip Transmission Line Suitable for Nonreciprocal Gyromagnetic Device Applications," *IEEE Trans. Microw. Theory Tech.*, vol. 17, no. 12, pp. 1087–1090, 1969.

[4] Y. Xu and R. G. R. G. Bosisio, "A study of planar Goubau lines (PGLs) for millimeter- and submillimeter-wave integrated circuits (ICs)," *Microw. Opt. Technol. Lett.*, vol. 43, no. 4, pp. 290–293, Nov. 2004.

[5] G. Goubau, "Surface waves and their application to transmission lines," *J. Appl. Phys.*, vol. 21, no. 11, pp. 1119–1128, 1950.

[6] M. F. Bauwens, N. Alijabbari, A. W. Lichtenberger, N. S. Barker, and R. M. Weikle, "A 1.1 THz micromachined on-wafer probe," *IEEE MTT-S Int. Microw. Symp. Dig.*, 2014.

[7] A. Treizebré, B. Bocquet, Y. Xu, and R. G. Bosisio, "New THz excitation of planar Goubau line," *Microw. Opt. Technol. Lett.*, vol. 50, no. 11, pp. 2998–3001, Nov. 2008.

[8] D. B. Rutledge, D. P. Neikirk, and D. P. Kasilingam, "Integrated-Circuit Antennas," in *Infrared and millimeter waves*, vol. 10, New York: Academic, 1983.

[9] M. Riaziat, R. Majidi-Ahy, and I. Feng, "Propagation Modes and Dispersion characteristics of CPW," vol. 38, no. 3, 1990.

[10] N. Fuse, T. Takahashi, Y. Ohki, R. Sato, M. Mizuno, and K. Fukunaga, "Terahertz Spectroscopy as a New Tool for Insulating Material Analysis and Condition Monitoring," *IEEE Insul. Mag.*, vol. 27, no. 3, pp. 26–35, 2011.

[11] R. B. Marks, "A Multiline Method of Network Analyzer Calibration," *IEEE Trans. Microw. Theory Tech.*, vol. 39, no. 7, pp. 1205–1215, 1991.

[12] J. Cabello-Sánchez, H. Rodilla, V. Drakinskiy, and J. Stake, "Multiline TRL Calibration Standards for S-parameter Measurement of Planar Goubau Lines from 0.75 THz to 1.1 THz," *IEEE MTT-S Int. Microw. Symp. Dig.*, 2018.

[13] Jingjing, S. Alexandrou, and T. Y. Hsiang, "Attenuation characteristics of coplanar waveguides at subterahertz frequencies," *IEEE Trans. Microw. Theory Tech.*, vol. 53, no. 11, pp. 3281–3287, Nov. 2005.

Paper C

On-Chip Characterization of High-Loss Liquids between 750 GHz and 1100 GHz

J. Cabello-Sánchez, V. Drakinskiy, J. Stake and H. Rodilla

IEEE Transactions on Terahertz Science and Technology
vol. 11, no. 1, Jan. 2021,
 DOI: 10.1109/TTHZ.2020.3029503

On-Chip Characterization of High-Loss Liquids between 750 GHz and 1100 GHz

Juan Cabello-Sánchez, *Student Member, IEEE,* Vladimir Drakinskiy, Jan Stake, *Senior Member, IEEE,* Helena Rodilla, *Senior Member, IEEE*

***Abstract*—Terahertz spectroscopy is a promising tool for analyzing the picosecond dynamics of biomolecules, which is influenced by surrounding water molecules. However, water causes extreme losses to terahertz signals, preventing sensitive measurements at this frequency range. Here, we present sensitive on-chip terahertz spectroscopy of highly lossy aqueous solutions using a vector network analyzer, contact probes, and a coplanar waveguide with a 0.1 mm wide microfluidic channel. The complex permittivities of various deionized water/isopropyl alcohol concentration are extracted from a known reference measurement across the frequency range 750–1100 GHz and agrees well with literature data. The results prove the presented method as a high-sensitive approach for on-chip terahertz spectroscopy of high-loss liquids, capable of resolving the permittivity of water.**

***Index Terms*—Coplanar waveguides (CPW), isopropyl alcohol (IPA), material properties, microfluidic channels, on-wafer measurements, permittivity, scattering parameters, terahertz spectroscopy, vector network analyzers (VNA), water**

I. Introduction

Terahertz (THz) spectroscopy is an indispensable tool to analyze light-weight molecules with applications in astronomy and chemistry. With new technological developments, the application of THz technology has extended to fields as diverse as security [1], communications [2], pharmaceutical control [3], medicine and biology [4]. In biology, THz waves have shown to be a relevant method for studying picosecond dynamics of biomolecules [5], [6], predicted to be key for their biological function [7] in which water plays an important role [8]. Aqueous samples have been measured with time-domain spectroscopy (TDS), one of the most common THz spectroscopy methods, with free-space transmission [9], free-space reflection [10], and on-chip setups [11], [12]. However, despite having a relatively high dynamic range, necessary for measuring high-loss samples, the low time-averaged power and wide bandwidth typically yield measurements with a low signal-to-noise ratio (SNR), limiting the smallest detectable signal change [13]. The low SNR further plummets when measuring high-loss aqueous samples (around 100 dB/mm [9]) in higher-loss chip setups, hindering pure water measurements at frequencies above 0.5 THz [12], or having to avoid liquid sample in the region with the most intense electric field to minimize losses [11], [14], but sacrificing sensitivity.

A promising method for obtaining high SNR for on-chip applications is measuring S-parameters using vector network analyzers (VNA), a common measuring method at microwave and millimeter-wave frequencies. This method is based on an electronic heterodyne technique, and benefits from having first-class frequency resolution ($\sim$ 1 Hz), about 20 dB higher dynamic range than TDS systems at 1 THz [15], traceability to the International System of Units [16], and can use calibration techniques to move the reference plane to the region of interest [17]; whereas the downside is that the bandwidth is limited to a waveguide band. The frequency range of VNA measurements applied to biology has been typically restricted to microwave [18] and millimeter-wave frequencies [19], [20]. However, recent development in heterodyne technology has increased the maximum frequency of VNA analysis up to 1.5 THz [21] in rectangular waveguides, and up to 1.1 THz for on-chip measurements using contact probes [22]. Contact probes offer an efficient way to guide the generated power directly into the sensing chip (compared to free-space coupling), thus increasing the sensibility of the method.

In this letter, we demonstrate the use of a vector network analyzer and contact probes for THz spectroscopy of high-loss aqueous samples contained in a chip. We describe the design of the low-loss sensing waveguide and its fabrication, the measurement setup, and how the complex refractive index was extracted from the measured complex transmission coefficient. This is a first step towards a miniaturized chip sensor for high-loss liquid samples at THz frequencies.

II. Method

For sensing liquid samples on a chip, we used a coplanar waveguide (CPW) [23], which provides easy interfacing with ground-signal-ground probes (Fig. 1.a). The CPW was designed to suit both the measurement probe's pitch (25 µm) and characteristic impedance (50 Ω) [22], yielding a central strip width of 23.5 µm and a ground separation of 1.5 µm. The CPW was designed on a ultra-thin 23 µm thick polyethylene terephthalate (PET) film substrate ($\epsilon' = 3.15$ and $\tan(\delta) = 0.017$ at 1 THz [24]), to avoid power leakage [25] to undesirable substrate modes [26]. The CPWs and their dedicated calibration standards were fabricated using e-beam lithography and evaporation of 20 nm Ti and 350 nm Au on top of the PET substrate.

Manuscript received July 17, 2020; revised September 5, 2020; accepted October 1, 2020. This work was supported by the Swedish Research Council (Vetenskapsrådet) under grant 2015-03981 , and Knut and Alice Wallenberg Foundation under grant 2014.0275.

Juan Cabello-Sánchez, Vladimir Drakinskiy, Jan Stake and Helena Rodilla are with the Terahertz and Millimetre Wave Laboratory, Chalmers University of Technology, SE-412 96 Gothenburg, Sweden. (e-mail: juancab@chalmers.se; vladimir.drakinskiy@chalmers.se; jan.stake@chalmers.se; rodilla@chalmers.se)

Color versions of one or more of the figures in this article are available online at http://ieeexplore.ieee.org.

Digital Object Identifier 10.1109/TTHZ.2020.3029503

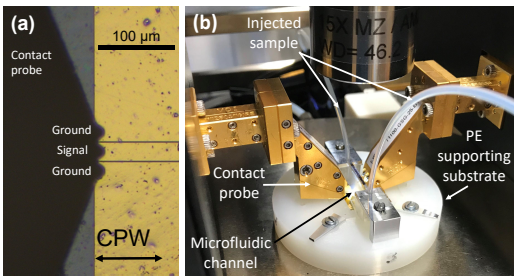

Fig. 1. (a) Micrograph of the CPW being excited by the ground-signal-ground probe. (b) Photograph of measurement setup during measurements.

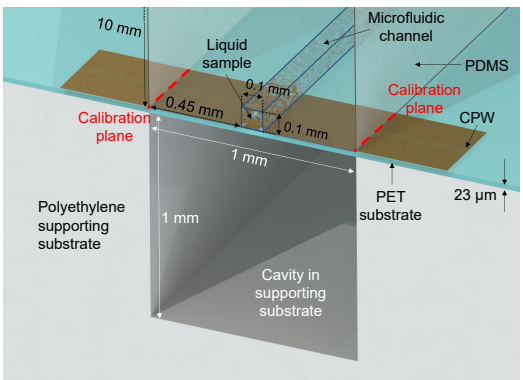

Fig. 2. Illustration of the cross-section of the microfluidic channel filled with sample intersecting the CPW.

The PET substrate containing the CPWs is held on top of a polyethylene supporting substrate to avoid coupling with the probe station's metal chuck during the measurements (Fig. 1.b). The polyethylene supporting substrate had a 1 mm deep and 1 mm long air cavity under the measured CPW, suspending it on air (Fig. 2). On top of the PET substrate, an interchangeable polydimethylsiloxane (PDMS) microfluidic channel was clamped to the polyethylene supporting substrate. The microfluidic channel was designed to have a 100 µm wide square cross-section, whereas the cross-section of the PDMS containing the channel is 1 mm wide by 10 mm tall (Fig. 2). To deliver the sample into the microfluidic channel, input and output tubings were connected to the microfluidic channel.

We measured the complex transmission coefficient, $\hat{T}_s$, between 0.75 THz and 1.1 THz using a VNA Keysight N5242A connected to two VDI WR1.0SAX frequency extenders [27], having a typical/minimum dynamic range of 65/45 dB, respectively, and a continuous wave signal power higher than −40 dBm. To couple the signal to the sensing chip, we used DMPI T-Wave ground-signal-ground probes [22]. We used dedicated multi-line TRL [28] calibration structures to set the calibration plane at the air-PDMS interface (Fig. 2).

The aqueous samples consist of propan-2-ol (IPA) in deionized-water (DI-H_2O) with different concentrations—0, 10, 20, 30, 40, and 50% of IPA in volume. The samples were pumped into the microfluidic channel from higher to lower concentration of IPA through the input tube using a syringe and flushing air between samples. The pressure was adjusted to atmospheric pressure by removing the syringe momentarily after introducing each sample. The probes were kept in contact with the chip throughout all measurements to minimize probing position uncertainty. Each sample was measured five times in consecutive VNA sweeps with an intermediate frequency bandwidth of 50 Hz.

The effective refractive index of the sample-loaded CPW ($\hat{n}_e = n_e - j\kappa_e$) was calculated by comparing the measured transmission with a reference measurement, $\hat{T}_r$ (average of five measurements with DI-water as sample), following the equation:

$$\hat{n}_e = \hat{n}_r - \frac{\ln\left[\hat{T}_s/\hat{T}_r\right]}{jk_0 l_s} \tag{1}$$

where k_0 is the vacuum wavenumber, l_s is the effective sample length, and $\hat{n}_r$ is the effective refractive index of the reference. $\hat{n}_r$ was obtained from analytical expressions for multilayered substrates on CPWs [29] and using a double Debye model for water [9] in order to include the frequency-dependent permittivity.

Finally, the sample's refractive index $\hat{n}_s$ was found from measured CPW's effective refractive index, $\hat{n}_e$, by using the same analytical expressions for multilayered substrates on CPWs [29]. According to it, the equation relating the sample permittivity with the CPW's effective permittivity is:

$$\begin{aligned}\hat{n}_e^2 = \hat{\epsilon}_e = 1 + \frac{1}{2}(\hat{n}_s^2 - 1)\frac{K(k)K(k_s')}{K(k')K(k_s)} + \\ + \frac{1}{2}(\hat{n}_{sub}^2 - 1)\frac{K(k)K(k_{sub}')}{K(k')K(k_{sub})}\end{aligned} \tag{2}$$

where K is the complete elliptical integral of the first kind, and k, k', k_s, k_s', k_{sub}, k_{sub}', are terms depending on the geometry of the CPW cross-section, superstrate (sample) and substrate, respectively [29]. The analytical expression (eq. 2) agrees well with more detailed 3D electromagnetic simulations of the multilayered CPW.

III. Results

We measured the transmission of a 1 mm long CPW with the PDMS microfluidic channel containing IPA/DI water solutions from 0.75 THz to 1.1 THz. For DI-water, the typical insertion loss was in the order of 25 dB. Fig. 3a-b shows the phase and magnitude, respectively, of the transmission for each sample normalized to the reference measurement (DI-water). Solid lines represent the average of five successive measurements, whereas the shadows represent their standard deviation. Both the normalized magnitude and phase consistently decrease for increasing IPA concentration, as expected from literature values [9], [30]. The artifacts observed around 0.95 THz and 1 THz, which appear as resonances in both magnitude and phase of the transmission, were also observed without any microfluidic channel. A possible explanation is parasitic probe-to-probe coupling effects or calibration artifacts [31].

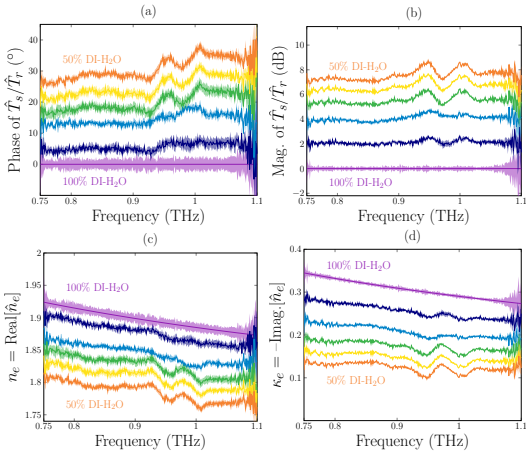

Fig. 3. Transmission measurements can resolve magnitude and phase differences between high-loss aqueous samples. Transmission (a) phase difference, and (b) power ratio with respect to reference measurement for the IPA/DI-H_2O samples (from 50% to 100% DI-H_2O in steps of 10%). (c) Real and (d) imaginary part of effective refractive indices of the CPW with samples. Lines indicate the mean of five measurements, whereas shadows indicate the standard deviation.

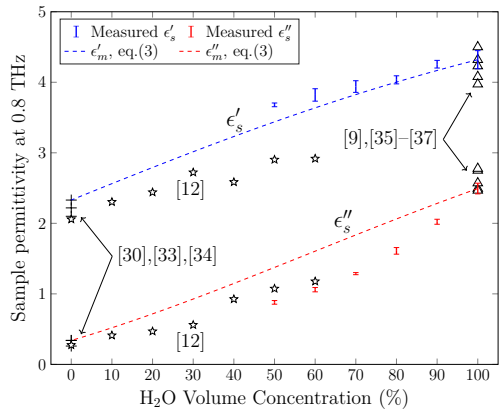

Fig. 4. Obtained sample permittivities show consistent change with varying water concentration. Permittivity of IPA/DI-H_2O samples vs. water concentration at 0.8 THz for this work (blue and red errorbars for 95% confidence interval) and literature values. Literature values of (+) IPA [30], [33], [34], (△) water [9], [35]–[37], and (☆) IPA/H_2O mixtures measured with a similar on-chip method [12] are plotted. The dashed lines show Bruggeman's model approximation for the change in water concentration, based in eq. (3).

The measurements' noise increases noticeably after 1.05 THz due to a drop in the dynamic range at the end of the frequency extender band. The relative error shows to be smaller for κ_e than for n_e, implying that in this case, smaller sample changes can be detected with attenuation measurements than with phase measurements. For water measurements the SNR was typically higher than 25 dB.

The real and imaginary effective refractive indices are shown in Fig. 3.c-d, where all high-loss samples have been successfully resolved. A relatively large effective length l_s = 250 µm was used since part of the liquid was found to extend between the PDMS and CPW substrate. Fig. 4 shows the samples' extracted real and imaginary permittivities at 0.8 THz versus sample DI-water concentration, showing error bars with 95% confidence interval. Both the real and imaginary parts of the permittivities change consistently with the changes of IPA concentration. The analytically extracted sample permittivities are also plotted with the permittivity of the IPA/water mixtures using literature values, using a modified Bruggeman's approximation for binary mixtures of polar liquids [32], with equation:

$$\left[\frac{\epsilon_m - \epsilon_{H_2O}}{\epsilon_{IPA} - \epsilon_{H_2O}}\right]\left[\frac{\epsilon_{IPA}}{\epsilon_m}\right]^{1/3} = 1 - \left[a - (a-1)\alpha_{H_2O}\right]\alpha_{H_2O} \quad (3)$$

where ϵ_{H_2O} and ϵ_{IPA} are literature values of the permittivities of water [9] and IPA [30] respectively, α_{H_2O} is the volume concentration of water, ϵ_m the permittivity of the mixture, and $a = 1.33$ is the fitting factor for propanol-water samples [32].

IV. Conclusion

This letter presents an on-chip dielectric spectroscopy method capable of measuring high-loss aqueous samples enabled by VNA and ground-signal-ground probes. Similar attempts of broadband measurements of aqueous solutions with TDS had problems resolving the complex refractive index for high water content solutions at frequencies higher than 0.5 THz [12] or lost sensitivity from not placing sample where the sensor's field is strongest [11]. The main reasons why the presented method could measure aqueous samples sensitively is due to (1) a higher coupling efficiency when exciting the CPWs using the contact probes compared to other methods which couple a free-space beam into the substrate via an antenna; (2) the higher average power of continuous-wave THz signals produced by the VNA compared to other pulsed methods, like TDS; (3) a low-loss design of the CPW. The high dynamic range (typically 50 dB at calibration plane) allows to measure water with a sample length up to approximately 0.6 mm. Some drawbacks of this method are that (1) is limited to frequencies up to 1.1 THz, due to lack of contact probes at higher frequencies; (2) being limited to rectangular waveguide bands for a given setup, and (3) a higher cost. In perspective, this method is a first step towards a miniaturized system for sensing high-loss aqueous samples at THz frequencies, which could provide an integrated, accurate, and controlled platform to study fundamental biological phenomena in their native environment.

Acknowledgment

The authors would like to thank Mr. Mats Myremark for machining parts for the measurement setup and Dr. Kiryl Kustanovich for helping to fabricate the microfluidic channel. The devices were fabricated and measured in the Nanofabrication Laboratory and Kollberg Laboratory, respectively, at Chalmers University of Technology, Gothenburg, Sweden.

REFERENCES

[1] R. Appleby and R. N. Anderton, "Millimeter-wave and submillimeter-wave imaging for security and surveillance," *Proceedings of the IEEE*, vol. 95, no. 8, pp. 1683–1690, 2007, doi: 10.1109/JPROC.2007.898832.

[2] H. J. Song and T. Nagatsuma, "Present and future of terahertz communications," *IEEE Transactions on Terahertz Science and Technology*, vol. 1, no. 1, pp. 256–263, 2011, doi: 10.1109/TTHZ.2011.2159552.

[3] J. A. Zeitler, P. F. Taday, D. A. Newnham, M. Pepper, K. C. Gordon, and T. Rades, "Terahertz pulsed spectroscopy and imaging in the pharmaceutical setting - a review," *Journal of Pharmacy and Pharmacology*, vol. 59, no. 2, pp. 209–223, 2 2007, doi: 10.1211/jpp.59.2.0008.

[4] E. Pickwell and V. P. Wallace, "Biomedical applications of terahertz technology," *Journal of Physics D: Applied Physics*, vol. 39, no. 17, 2006, doi: 10.1088/0022-3727/39/17/R01.

[5] G. Acbas, K. A. Niessen, E. H. Snell, and A. G. Markelz, "Optical measurements of long-range protein vibrations," *Nature Communications*, vol. 5, pp. 1–7, 2014, doi: 10.1038/ncomms4076.

[6] I. V. Lundholm, H. Rodilla, W. Y. Wahlgren, A. Duelli, G. Bourenkov, J. Vukusic, R. Friedman, J. Stake, T. Schneider, and G. Katona, "Terahertz radiation induces non-thermal structural changes associated with Fröhlich condensation in a protein crystal," *Structural Dynamics*, vol. 2, no. 5, 2015, doi: 10.1063/1.4931825.

[7] K. Henzler-Wildman and D. Kern, "Dynamic personalities of proteins," *Nature*, vol. 450, no. 7172, pp. 964–972, 12 2007, doi: 10.1038/nature06522.

[8] Y. Xu and M. Havenith, "Perspective: Watching low-frequency vibrations of water in biomolecular recognition by THz spectroscopy," *Journal of Chemical Physics*, vol. 143, no. 17, p. 224511, 2015, doi: 10.1063/1.4934504.

[9] J. T. Kindt and C. A. Schmuttenmaer, "Far-Infrared Dielectric Properties of Polar Liquids Probed by Femtosecond Terahertz Pulse Spectroscopy," *The Journal of Physical Chemistry*, 1996, doi: 10.1021/jp960141g.

[10] L. Thrane, R. H. Jacobsen, P. U. Jepsen, and S. R. Keiding, "THz reflection spectroscopy of liquid water," *Chemical Physics Letters*, vol. 240, no. 4, pp. 330–333, 1995, doi: 10.1016/0009-2614(95)00543-D.

[11] J. Kitagawa, T. Ohkubo, M. Onuma, and Y. Kadoya, "THz spectroscopic characterization of biomolecule/water systems by compact sensor chips," *Applied Physics Letters*, vol. 89, no. 4, p. 41114, 2006, doi: 10.1063/1.2236295.

[12] M. Swithenbank, A. D. Burnett, C. Russell, L. H. Li, A. G. Davies, E. H. Linfield, J. E. Cunningham, and C. D. Wood, "On-Chip Terahertz-Frequency Measurements of Liquids," *Analytical Chemistry*, vol. 89, no. 15, pp. 7981–7987, 8 2017, doi: 10.1021/acs.analchem.7b01235.

[13] M. Naftaly and R. Dudley, "Methodologies for determining the dynamic ranges and signal-to-noise ratios of terahertz time-domain spectrometers," *Optics Letters*, vol. 34, no. 8, p. 1213, 4 2009, doi: 10.1364/ol.34.001213.

[14] T. Ohkubo, M. Onuma, J. Kitagawa, and Y. Kadoya, "Micro-strip-line-based sensing chips for characterization of polar liquids in terahertz regime," *Applied Physics Letters*, vol. 88, no. 21, p. 212511, 5 2006, doi: 10.1063/1.2207989.

[15] D. K. George, A. Charkhesht, and N. Q. Vinh, "New terahertz dielectric spectroscopy for the study of aqueous solutions," *Review of Scientific Instruments*, vol. 86, no. 12, p. 123105, 2015, doi: 10.1063/1.4936986.

[16] N. M. Ridler and R. G. Clarke, "Establishing Traceability to the International System of Units for Scattering Parameter Measurements from 750 GHz to 1.1 THz," *IEEE Transactions on Terahertz Science and Technology*, vol. 6, no. 1, pp. 2–11, 2016, doi: 10.1109/TTHZ.2015.2502068.

[17] R. F. Bauer and P. Penfield, "De-Embedding and Unterminating," *IEEE Transactions on Microwave Theory and Techniques*, vol. 22, no. 3, pp. 282–288, 1974, doi: 10.1109/TMTT.1974.1128212.

[18] P. Velez, L. Su, K. Grenier, J. Mata-Contreras, D. Dubuc, and F. Martin, "Microwave Microfluidic Sensor Based on a Microstrip Splitter/Combiner Configuration and Split Ring Resonators (SRRs) for Dielectric Characterization of Liquids," *IEEE Sensors Journal*, vol. 17, no. 20, pp. 6589–6598, 2017, doi: 10.1109/JSEN.2017.2747764.

[19] H. Rodilla, A. A. Kim, G. D. Jeffries, J. Vukusic, A. Jesorka, and J. Stake, "Millimeter-wave sensor based on a $\lambda/2$-line resonator for identification and dielectric characterization of non-ionic surfactants," *Scientific Reports*, vol. 6, no. October 2015, pp. 1–5, 2016, doi: 10.1038/srep19523.

[20] X. Bao, I. Ocket, J. Bao, J. Doijen, J. Zheng, D. Kil, Z. Liu, B. Puers, D. Schreurs, and B. Nauwelaers, "Broadband Dielectric Spectroscopy of Cell Cultures," *IEEE Transactions on Microwave Theory and Techniques*, vol. 66, no. 12, pp. 5750–5759, 2018, doi: 10.1109/TMTT.2018.2873395.

[21] D. Koller, S. Durant, C. Rowland, E. Bryerton, and J. Hesler, "Initial measurements with WM164 (1.1-1.5THz) VNA extenders," in *2016 41st International Conference on Infrared, Millimeter, and Terahertz Waves (IRMMW-THz)*, Copenhagen, 2016, pp. 1–2, doi: 10.1109/IRMMW-THz.2016.7758434.

[22] M. F. Bauwens, N. Alijabbari, A. W. Lichtenberger, N. S. Barker, and R. M. Weikle, "A 1.1 THz micromachined on-wafer probe," in *2014 IEEE MTT-S International Microwave Symposium (IMS2014)*, Tampa, FL, 2014, pp. 1–4, doi: 10.1109/MWSYM.2014.6848607.

[23] C. P. Wen, "Coplanar Waveguide: A Surface Strip Transmission Line Suitable for Nonreciprocal Gyromagnetic Device Applications," *IEEE Transactions on Microwave Theory and Techniques*, vol. 17, no. 12, pp. 1087–1090, 1969, doi: 10.1109/TMTT.1969.1127105.

[24] N. Fuse, T. Takahashi, Y. Ohki, R. Sato, M. Mizuno, and K. Fukunaga, "Terahertz Spectroscopy as a New Tool for Insulating Material Analysis and Condition Monitoring," *IEEE Insulating Magazine*, vol. 27, no. 3, pp. 26–35, 2011, doi: 10.1109/MEI.2011.5871366.

[25] J. Cabello-Sánchez, H. Rodilla, V. Drakinskiy, and J. Stake, "Transmission Loss in Coplanar Waveguide and Planar Goubau Line between 0.75 THz and 1.1 THz," in *2018 43rd International Conference on Infrared, Millimeter, and Terahertz Waves (IRMMW-THz)*, Nagoya, 2018, pp. 1–2, doi: 10.1109/IRMMW-THz.2018.8510326.

[26] D. B. Rutledge, S. E. Schwarz, and A. T. Adams, "Infrared and submillimetre antennas," *Infrared Physics*, vol. 18, no. 5-6, pp. 713–729, 1978, doi: 10.1016/0020-0891(78)90094-5.

[27] T. W. Crowe, B. Foley, S. Durant, K. Hui, Y. Duan, and J. L. Hesler, "VNA frequency extenders to 1.1 THz," in *2011 36th International Conference on Infrared, Millimeter, and Terahertz Waves (IRMMW-THz)*, Houston, TX, 2011, pp. 1–1, doi: 10.1109/irmmw-THz.2011.6105028.

[28] R. B. Marks, "A Multiline Method of Network Analyzer Calibration," *IEEE Transactions on Microwave Theory and Techniques*, vol. 39, no. 7, pp. 1205–1215, 1991, doi: 10.1109/22.85388.

[29] E. Chen and S. Y. Chou, "Characteristics of coplanar transmission lines on multilayer substrates: modeling and experiments," *IEEE Transactions on Microwave Theory and Techniques*, vol. 45, no. 6, pp. 939–945, 1997, doi: 10.1109/22.588606.

[30] Y. Yomogida, Y. Sato, R. Nozaki, T. Mishina, and J. Nakahara, "Comparative study of boson peak in normal and secondary alcohols with terahertz time-domain spectroscopy," *Physica B: Condensed Matter*, vol. 405, no. 9, pp. 2208–2212, 2010, doi: 10.1016/j.physb.2010.02.010.

[31] G. N. Phung, F. J. Schmuckle, R. Doerner, B. Kahne, T. Fritzsch, U. Arz, and W. Heinrich, "Influence of microwave probes on calibrated on-wafer measurements," *IEEE Transactions on Microwave Theory and Techniques*, vol. 67, no. 5, pp. 1892–1900, 2019, doi: 10.1109/TMTT.2019.2903400.

[32] S. M. Puranik, A. C. Kumbharkhane, and S. C. Mehrotra, "The static permittivity of binary mixtures using an improved bruggeman model," *Journal of Molecular Liquids*, vol. 59, no. 2-3, pp. 173–177, 1994, doi: 10.1016/0167-7322(93)00665-6.

[33] Y. Yomogida, Y. Sato, R. Nozaki, T. Mishina, and J. Nakahara, "Comparative dielectric study of monohydric alcohols with terahertz time-domain spectroscopy," *Journal of Molecular Structure*, vol. 981, no. 1-3, pp. 173–178, 2010, doi: 10.1016/j.molstruc.2010.08.002.

[34] M. Swithenbank, C. Russell, A. D. Burnett, L. H. Li, A. G. Davies, E. H. Linfield, J. E. Cunningham, and C. D. Wood, "Accurate parameter extraction from liquids measured using on-chip terahertz spectroscopy," in *International Conference on Infrared, Millimeter, and Terahertz Waves, IRMMW-THz*, Copenhagen, 2016, pp. 1–2, doi: 10.1109/IRMMW-THz.2016.7758409.

[35] P. U. Jepsen, U. Møller, and H. Merbold, "Investigation of aqueous alcohol and sugar solutions with reflection terahertz time-domain spectroscopy," *Optics Express*, vol. 15, no. 22, p. 14717, 2007, doi: 10.1364/OE.15.014717.

[36] D. J. Segelstein, "The complex refractive index of water," Ph.D. dissertation, Department of Physics, University of Missouri-Kansas City, 1981.

[37] N. Q. Vinh, M. S. Sherwin, S. J. Allen, D. K. George, A. J. Rahmani, and K. W. Plaxco, "High-precision gigahertz-to-terahertz spectroscopy of aqueous salt solutions as a probe of the femtosecond-to-picosecond dynamics of liquid water," *Journal of Chemical Physics*, vol. 142, no. 16, p. 164502, 2015, doi: 10.1063/1.4918708.

Juan Cabello-Sánchez (S' 17) was born in Madrid in 1992. He received the Bachelor diploma in Electrical Engineering and Computer Science (ABET-accredited) from the Technical University of Madrid, Spain, in 2015, and MSc in Wireless, Photonics and Space Engineering from Chalmers University of Technology, in Gothenburg, Sweden, in 2017.

From July 2017 he is pursuing his PhD in the THz and Millimetre-wave Laboratory at Chalmers University of Technology.

Vladimir Drakinskiy Vladimir Drakinskiy was born in Kurganinsk, Russia, in 1977. He received the Diploma degree in physics and informatics (with honors) from the Armavir State Pedagogical Institute, Armavir, Russia, in 2000, and the Postgraduate degree from Moscow State Pedagogical University, Moscow, Russia, in 2003.

From 2000 to 2003, he was a Junior Research Assistant in the Physics Department, Moscow State Pedagogical University. Since 2003, he has been in the Department of Microtechnology and Nanoscience, Chalmers University of Technology, Gothenburg, Sweden. During 2003–2005, he was responsible for mixer chips fabrication for the Herschel Space Observatory. Since 2008, he has been a Research Engineer with the Department of Microtechnology and Nanoscience, Chalmers University of Technology. He is currently responsible for terahertz Schottky diodes process line at MC2, Chalmers University of Technology. His research interests include microfabrication and nanofabrication techniques, detectors for submillimeter and terahertz ranges, and superconducting thin films.

Jan Stake (S' 95–M' 00–SM' 06) was born in Uddevalla, Sweden, in 1971. He received the M.Sc. degree in electrical engineering and the Ph.D. degree in microwave electronics from the Chalmers University of Technology, Goteborg, Sweden, in 1994 and 1999, respectively.

In 1997, he was a Research Assistant with the University of Virginia, Charlottesville, VA, USA. From 1999 to 2001, he was a Research Fellow with the Millimetre Wave Group, Rutherford Appleton Laboratory, Didcot, U.K. He was then a Senior RF/Microwave Engineer with Saab Combitech Systems AB, until 2003. From 2000 to 2006, he held different academic positions with the Chalmers University of Technology and, from 2003 to 2006, was also the Head of the Nanofabrication Laboratory, Department of Microtechnology and Nanoscience, MC2. During Summer 2007, he was a Visiting Professor with the Submillimeter Wave Advanced Technology Group, Caltech/JPL, Pasadena, CA, USA. He is currently a Professor and the Head of the Terahertz and Millimetre Wave Laboratory, Chalmers University of Technology. He is also a Cofounder of Wasa Millimeter Wave AB, Goteborg, Sweden. His research interests include graphene electronics, high frequency semiconductor devices, THz electronics, submillimeter wave measurement techniques ("THz metrology"), and THz in biology and medicine.

Prof. Stake served as Editor-in-Chief for the IEEE TRANSACTIONS ON TERAHERTZ SCIENCE AND TECHNOLOGY from 2016 to 2018.

Helena Rodilla (M' 16–SM' 20) was born in Salamanca, Spain, in 1982. She received the B.S. and Ph.D. degrees in Physics from the University of Salamanca, Salamanca, Spain, in 2006 and 2010, respectively.

From 206 to 2010, she was with the Electronics Group, Department of Applied Physics, University of Salamanca, Spain, where her research interest was semiconductor physics. From 2011 to 2013 she was Postdoctoral Researcher with the Microwave Electronics Laboratory, Department of Microtechnology and Nanoscience (MC2), Chalmers University of Technology, Gothenburg, Sweden, where she worked on very low-noise InP HEMTs for cryogenic low noise amplifiers. Since 2013 she has been with the Terahertz and Millimetre Wave Laboratory, MC2, Chalmers University of Technology, Gothenburg, Sweden, where she became Associate Professor in 2020. Her current research interests include the use of millimeter wave and terahertz technology in life science applications, sensing and on-wafer terahertz measurements.